

Non-Darcian flow in fibre-reinforced biological tissues

Original

Non-Darcian flow in fibre-reinforced biological tissues / Grillo, Alfio; Carfagna, Melania; Federico, Salvatore. - In: MECCANICA. - ISSN 0025-6455. - STAMPA. - 52:14(2017), pp. 3299-3320. [10.1007/s11012-017-0679-0]

Availability:

This version is available at: 11583/2670694 since: 2020-06-03T20:17:43Z

Publisher:

Springer

Published

DOI:10.1007/s11012-017-0679-0

Terms of use:

This article is made available under terms and conditions as specified in the corresponding bibliographic description in the repository

Publisher copyright

Springer postprint/Author's Accepted Manuscript

This version of the article has been accepted for publication, after peer review (when applicable) and is subject to Springer Nature's AM terms of use, but is not the Version of Record and does not reflect post-acceptance improvements, or any corrections. The Version of Record is available online at: <http://dx.doi.org/10.1007/s11012-017-0679-0>

(Article begins on next page)

Non-Darcian Flow in Fibre-Reinforced Biological Tissues

Alfio Grillo · Melania Carfagna · Salvatore Federico

Received: date / Accepted: date

DOI: 10.1007/s11012-017-0679-0. Available online: May 17, 2017

Journal: *Meccanica* (2017) 52: 3299-3320 (Springer)

Abstract Under suitable conditions, the motion of a fluid in a porous medium can be studied by assuming the validity of Darcy's law. Since many biological tissues can be thought of as porous media, Darcy's law is invoked in several biomechanical contexts, like the transport of the chemical species needed for the metabolism of tissue cells. Although Darcy's law supplies physically sound results in many circumstances, there may be cases in which the dynamic behaviour of a biological fluid deviates from the Darcian one. The scope of this work is to analyse some possible consequences of such deviations, with emphasis on the fluid velocity and pressure, which, in turn, influence the health and correct functioning of the tissue cells. In particular, our study addresses the flow of an interstitial fluid through a fibre-reinforced tissue, in which the fibres are oriented statistically. We take articular cartilage as a representative tissue of this type, and study the deviation from Darcy's law known as "Forchheimer's correction". Moreover, we introduce two models of tissue

permeability, which lead to discrepant results when the fluid velocity is described by Darcy's law. We show, however, that the discrepancies in the description of the flow can be reduced if Forchheimer's correction is applied.

Keywords Biological tissue · Porous medium · Biphase material · Fibre-reinforcement · Composite materials · Transverse isotropy · Darcy's law · Forchheimer's correction

1 Introduction

Many biological tissues, such as articular cartilage [48, 49, 35, 34, 26], can be described as biphasic systems comprising a fluid and a solid phase. In the course of its life, a porous tissue responds to stimuli of various nature, among which the mechanical ones contribute to vary its shape and internal structure.

The fluid flowing through a tissue is affected by the tissue's structural variations, and changes its velocity and pressure accordingly. Since these changes are relevant for the tissue's health, it is important to understand the dynamics of biological fluids. In particular, the flow of the interstitial fluid in articular cartilage is related to the tissue's microstructure, which changes in time because of the deformation of the non-fibrous matrix (comprising mainly proteoglycans and chondrocytes) and the reorientation of the collagen fibres. Thus, the velocity of the fluid must be coupled with the deformation, and should reflect the evolution of the medium's anisotropy. At the tissue scale, the motion of the fluid is described by a velocity field, called filtration velocity, obtained by eliminating the velocity fluctuations associated with the pore scale heterogeneities of the flow, and multiplying the result by the

A. Grillo (Corresponding Author) · M. Carfagna
Dept of Mathematical Sciences (DISMA) "G.L. Lagrange",
Politecnico di Torino
Corso Duca degli Abruzzi 24, 10129, Torino, Italy
Tel.: +39-011-0907531
Fax: +39-011-0907599
E-mail: alfio.grillo@polito.it
E-mail: melania.carfagna@polito.it

S. Federico
Dept of Mechanical and Manufacturing Engineering, The
University of Calgary
2500 University Drive NW, Calgary, AB, T2N 1N4, Canada
E-mail: salvatore.federico@ucalgary.ca

fluid volumetric fraction (see [21, 22] for the definition of mass average of the pore scale velocity). In many cases of biomechanical interest, the fluid filtration velocity is linearly related to the pressure gradient applied to the fluid. Such hypothesis is at the basis of Darcy's law [20]. Apart from the description of the flow, Darcy's law is also used to compute the advection velocity by which nutrients and other chemicals are conveyed to the cells [8].

We emphasise that the standard formulation of Darcy's law stems from the assumption that the macroscopic inertial forces are negligible, the stress borne by the fluid is purely hydrostatic (no viscous stress is accounted for), and the dissipative forces exchanged among the tissue's constituents are balanced by the pressure gradient, multiplied by the volumetric fraction of the fluid phase [20, 1]. The second-order tensor relating the pressure gradient to the filtration velocity is referred to as *hydraulic conductivity*, or *permeability*. More precisely, in the jargon of Porous Media, the "hydraulic conductivity" is the second-order tensor obtained by dividing the permeability tensor by the fluid viscosity [4], while, in Biomechanics, "(hydraulic) permeability" and "hydraulic conductivity" are usually regarded as synonyms, and are both expressed in $\text{mm}^4\text{N}^{-1}\text{s}^{-1}$ [1]. In the sequel, we follow the terminology used in Biomechanics.

Several anisotropic permeability models have been proposed to couple the fluid filtration velocity with the deformation of the matrix [42, 1]. Also, as deduced in the studies of Maroudas and Bulloch [31], collagen fibres contribute to the permeability of articular cartilage, and exert a resistance to the flow, which adds itself to that supplied by the matrix. This argument has been demonstrated under no or small deformations in [15, 14]. In these works, it is shown that the interstitial fluid flows more easily along the fibres than it does across them. The effect of the fibres on the permeability has also been studied under large deformations [12, 37, 38, 47].

Even though the models discussed so far are purely Darcian, there are cases in which Darcy's law may cease to describe the flow adequately. A thorough discussion on this subject can be found in [4]. There exist, in fact, two typical situations in which Darcy's law should be replaced by other descriptions of the flow. One of these occurs when the viscous stress tensor has to be considered in the momentum balance law of the fluid and, in this case, one speaks of Brinkman's equation [4]. The other one, instead, leads to Forchheimer's correction of Darcy's law [4, 5], and arises when the relationship between the fluid filtration velocity and the pressure gradient acquires a quadratic term in the filtration velocity, with a coefficient depending on the mi-

crostructure of the porous medium [5]. We remark that Brinkman's equation is necessary when boundary effects must be included in the description of the flow, and that Forchheimer's correction is suggested when the flow is subjected to inertial effects [27]. It should be noticed, however, that these inertial effects are the microscopic ones, since Forchheimer's correction is derived under the hypothesis of negligible macroscopic inertial forces in the momentum balance law (see the derivation in Section 3). In other words, Forchheimer's correction is the representation at the tissue scale of microscopic inertial terms that contribute to the drag forces exchanged by the tissue's constituents [5].

In this work we study Forchheimer's correction within a nonlinear and anisotropic model of articular cartilage, which is regarded as a hyperelastic, fibre-reinforced tissue, undergoing finite deformations and in which the fibres are oriented statistically. We give ourselves this task for several reasons:

- (i) To improve the understanding of Forchheimer's correction in the biomechanical context. Indeed, to the best of our knowledge, in Biomechanics Forchheimer's correction has not been investigated until recently (one paper we are aware of is that of Khaled et al. [27]), whereas it is commonly employed in completely different contexts, like hydrogeology, for problems in which the deformability of the porous medium hosting the flow is usually disregarded.
- (ii) To enrich the description of the flow of biological fluids. Indeed, even though in Biomechanics it is usually believed that Darcy's law is sufficient to model the flow, there can be situations (for example, in the benchmark tests performed to estimate the elastic and flow properties of articular cartilage) in which particularly severe loading conditions may trigger the microscopic inertial effects that call for Forchheimer's correction.
- (iii) Since Forchheimer's correction decreases the magnitude of the fluid filtration velocity and increases the fluid pressure, we use it to be more conservative in establishing the pressure threshold above which the tissue health may be compromised.
- (iv) Forchheimer's correction introduces coefficients which may be tuned to fit experimental data. We show, indeed, that a partial agreement between two different permeability models, presented in [1] and [12], respectively, each with its own rationale, can be achieved by tuning a coefficient referred to as "trial friction factor" (see Section 5.1).

The work is organised as follows. In Section 2, we present the derivation of the model equations. In Section 3, we review Darcy's law and Forchheimer's correc-

tion. In Section 4, we present the constitutive framework. In Section 5, we describe the benchmark tests and the related numerical results. In Section 6, we summarise the main achievements of our work.

2 Biphasic Model of Fibre-Reinforced Hydrated Soft Tissues

Following [15, 47], we assume that a Representative Elementary Volume (REV) exists, i.e., we admit that a region of space of constant size can be defined, whose characteristic length scale is sufficiently smaller than that of the tissue's coarse-scale heterogeneities, and sufficiently larger than that of the fine-scale ones [21]. The REV is partitioned into sub-regions, and each sub-region is occupied by one constituent of the tissue. The ratio between the measure of the sub-volume of the REV filled with the interstitial fluid and the measure of the REV is referred to as the fluid phase volumetric fraction, ϕ_f . Under the assumption of saturation, we denote by $\phi_s = 1 - \phi_f$ the volumetric fraction of the solid phase. The portion of REV filled with the solid phase is subdivided into two disjoint sub-regions, occupied by the matrix and the fibres with volumetric fractions ϕ_{0s} and ϕ_{1s} , respectively [47]. It holds that $\phi_{0s} + \phi_{1s} = \phi_s$, where ϕ_{0s} and ϕ_{1s} are expressed per unit volume of the REV.

2.1 Kinematics

As done in [47, 17, 9], we describe the kinematics of the considered biphasic system by adapting to our problem the theoretical framework developed for solid-fluid mixtures in [40, 41]. Thus, two smooth material manifolds, \mathcal{M}_s and \mathcal{M}_f , are introduced, representing the solid and the fluid phase, respectively. The manifold \mathcal{M}_s is embedded into the three-dimensional Euclidean space \mathcal{S} , where it occupies the region $\mathcal{B} \subset \mathcal{S}$, called reference configuration.

Given the interval of time $\mathcal{J} \subset \mathbb{R}$ over which the system's evolution is observed, the motion χ of the solid phase maps \mathcal{B} into the *current configuration* $\chi(\mathcal{B}, t) \subset \mathcal{S}$. While in [40, 41] the “points” of the manifolds \mathcal{M}_s are the particles of the solid constituent of a biphasic mixture, in the present framework each particle of \mathcal{M}_s includes both the matrix and the fibres, and both constituents are constrained to share the same motion χ . The motion of the fluid is represented by a one-parameter family of smooth embeddings \mathbf{f} such that, at each $t \in \mathcal{J}$, the fluid particle $\mathcal{X}_f \in \mathcal{M}_f$ is embedded into the point $x \in \mathcal{S}$. The region $\mathcal{B}_t \subset \mathcal{S}$, at each point of which the solid and fluid particles coexist, is denoted

by $\mathcal{B}_t := \chi(\mathcal{B}, t) \cap \mathbf{f}(\mathcal{M}_f, t)$. By definition of \mathcal{B}_t it holds that $x = \chi(X, t) = \mathbf{f}(\mathcal{X}_f, t)$, for all $x \in \mathcal{B}_t$, with $X \in \mathcal{B}$ and $\mathcal{X}_f \in \mathcal{M}_f$.

For $x \in \mathcal{S}$, $T_x\mathcal{S}$ is the tangent space of \mathcal{S} attached at x , and $T\mathcal{S} = \sqcup_{x \in \mathcal{S}} T_x\mathcal{S}$ is the tangent bundle. Their duals are denoted by $T_x^*\mathcal{S}$ and $T^*\mathcal{S}$, respectively. Similarly, we define $T_X\mathcal{B}$ and $T_X^*\mathcal{B}$, with their bundles $T\mathcal{B}$ and $T^*\mathcal{B}$. Moreover, we define the tensor spaces of order $r + s$, where $r \geq 0$ and $s \geq 0$ are arbitrary positive integers [7, 12], as

$$[T\mathcal{S}]^r_s = \underbrace{T\mathcal{S} \otimes \dots \otimes T\mathcal{S}}_{r \text{ times}} \otimes \underbrace{T^*\mathcal{S} \otimes \dots \otimes T^*\mathcal{S}}_{s \text{ times}}, \quad (1a)$$

$$[T\mathcal{B}]^r_s = \underbrace{T\mathcal{B} \otimes \dots \otimes T\mathcal{B}}_{r \text{ times}} \otimes \underbrace{T^*\mathcal{B} \otimes \dots \otimes T^*\mathcal{B}}_{s \text{ times}}. \quad (1b)$$

For $x \in \mathcal{B}_t$ and $t \in \mathcal{J}$, we introduce the velocity vectors $\mathbf{v}_s(x, t) \in T_x\mathcal{S}$ and $\mathbf{v}_f(x, t) \in T_x\mathcal{S}$, associated with the solid and fluid phase, respectively, the relative velocity $\mathbf{w} = \mathbf{v}_f - \mathbf{v}_s \in T\mathcal{S}$ and the filtration velocity $\mathbf{q} := \phi_f \mathbf{w} = \phi_f(\mathbf{v}_f - \mathbf{v}_s) \in T\mathcal{S}$ (note that, in several of our past works, we used \mathbf{w} to denote the filtration velocity instead of \mathbf{q}). Using the jargon of Marsden and Hughes [32], we also define the velocity vector fields covering $\chi(\cdot, t)$ and $\mathbf{f}(\cdot, t)$, respectively, i.e., $\mathbf{u}_s(\cdot, t) : \mathcal{B} \rightarrow T\mathcal{S}$ and $\mathbf{u}_f(\cdot, t) : \mathcal{M}_f \rightarrow T\mathcal{S}$, which satisfy the equalities $\mathbf{v}_s(x, t) = \mathbf{u}_s(X, t) = \dot{\chi}(X, t)$ and $\mathbf{v}_f(x, t) = \mathbf{u}_f(\mathcal{X}_f, t) = \dot{\mathbf{f}}(\mathcal{X}_f, t)$, with the superimposed “dot” standing for partial differentiation with respect to time. Finally, we introduce the deformation gradient tensor of the solid phase, \mathbf{F} , i.e., the tangent map $T\chi(\cdot, t) = \mathbf{F}(\cdot, t) : T\mathcal{B} \rightarrow T\mathcal{S}$ of the solid phase motion $\chi(\cdot, t)$ [32]. For $X \in \mathcal{B}$ and $x = \chi(X, t)$, $\mathbf{F}(X, t) : T_X\mathcal{B} \rightarrow T_x\mathcal{S}$ is a linear map transforming vectors of $T_X\mathcal{B}$ into vectors of $T_x\mathcal{S}$, and can be defined through the directional derivative of $\chi(\cdot, t)$ at $X \in \mathcal{B}$ along some vector $\mathbf{U} \in T_X\mathcal{B}$, i.e., $\partial_{\mathbf{U}}\chi(X, t) = \mathbf{F}(X, t)\mathbf{U} \in T_x\mathcal{S}$. The determinant of \mathbf{F} is denoted by $J = \det(\mathbf{F})$ and is required to be strictly positive in order for χ to be admissible. We emphasise that, since the matrix and the fibres are assumed to share the same motion, χ , they also share the same velocity, \mathbf{v}_s (or \mathbf{u}_s), and the same deformation gradient tensor \mathbf{F} . Along with \mathbf{F} , we also introduce the right and the left Cauchy-Green deformation tensors, denoted by $\mathbf{C} = \mathbf{F}^T \cdot \mathbf{F} = \mathbf{F}^T \mathbf{g} \mathbf{F}$ and $\mathbf{b} = \mathbf{F} \cdot \mathbf{F}^T = \mathbf{F} \mathbf{G}^{-1} \mathbf{F}^T$, respectively, where $\mathbf{g} \in [T\mathcal{S}]_2^0$ and $\mathbf{G} \in [T\mathcal{B}]_2^0$ are the metric tensors associated with the spatial and material description of the system, respectively.

2.2 Balance Laws and Dissipation Inequality

We introduce the mass balance laws for the three constituents considered in the present model of articular

cartilage, i.e., matrix, fibres and fluid phase, with the corresponding mass densities ϱ_{0s} , ϱ_{1s} , and ϱ_f , which we regard here as constant (cf. e.g. [47]). In material formalism, these balance laws read

$$\dot{\Phi}_{\alpha s} = 0, \quad \alpha \in \{0, 1\}, \quad (2a)$$

$$\dot{J} + \text{Div } \mathbf{Q} = 0. \quad (2b)$$

where $\Phi_{\alpha s} := J\phi_{\alpha s}$ is the constant volumetric fraction of the α th solid constituent (i.e., matrix or fibres) in the reference configuration, and $\mathbf{Q} = J\mathbf{F}^{-1}\mathbf{q}$ is the *material filtration velocity*, i.e., the backward Piola transform of the filtration velocity \mathbf{q} . Note that the material form of the volumetric fraction of the solid phase, $\Phi_s = \Phi_{0s} + \Phi_{1s}$, is constant in time too, whereas the material form of the fluid phase volumetric fraction is given by $\Phi_f = J - \Phi_s$.

Next, we introduce the momentum balance laws, under the hypothesis that inertial and external body forces are negligible, i.e.,

$$\text{div } \boldsymbol{\sigma}_s + \boldsymbol{\pi}_s = \mathbf{0}, \quad (3a)$$

$$\text{div } \boldsymbol{\sigma}_f + \boldsymbol{\pi}_f = \mathbf{0}, \quad (3b)$$

where $\boldsymbol{\pi}_s$ and $\boldsymbol{\pi}_f$ represent the force densities due to the momentum exchange between the solid and the fluid constituent, and

$$\boldsymbol{\sigma}_s = -\phi_s p \mathbf{g}^{-1} + \boldsymbol{\sigma}_{sc}, \quad (4a)$$

$$\boldsymbol{\sigma}_f = -\phi_f p \mathbf{g}^{-1} = -(1 - \phi_s) p \mathbf{g}^{-1} \quad (4b)$$

are the Cauchy stress tensors associated with the solid and the fluid phase, respectively. In (4a) and (4b), p is a hydrostatic pressure called *pore pressure*, and $\boldsymbol{\sigma}_{sc}$ is the *constitutive part* of $\boldsymbol{\sigma}_s$. Since the system under study is closed with respect to momentum, the condition $\boldsymbol{\pi}_s + \boldsymbol{\pi}_f = \mathbf{0}$ has to apply. Hence, by adding together (3a) and (3b), one obtains

$$\text{div } \boldsymbol{\sigma} \equiv \text{div}(-p \mathbf{g}^{-1} + \boldsymbol{\sigma}_{sc}) = \mathbf{0}, \quad (5a)$$

$$-\mathbf{g}^{-1} \text{grad}(\phi_f p) + \boldsymbol{\pi}_f = \mathbf{0}, \quad (5b)$$

where $\boldsymbol{\sigma} = \boldsymbol{\sigma}_s + \boldsymbol{\sigma}_f$ is the total Cauchy stress tensor. For the system under study, the local dissipation, \mathfrak{D} , computed per unit volume of \mathcal{B}_t , is given by

$$\mathfrak{D} = -\boldsymbol{\pi}_{fd} \cdot \frac{\mathbf{q}}{\phi_f} \geq 0, \quad (6)$$

where the term $\boldsymbol{\pi}_{fd} := \boldsymbol{\pi}_f - p \mathbf{g}^{-1} \text{grad } \phi_f$, i.e., the dissipative force density [20], permits to reformulate (5b) as (see e.g. [20, 6])

$$\boldsymbol{\pi}_{fd} = \phi_f \mathbf{g}^{-1} \text{grad } p. \quad (7)$$

3 Darcy's Law and Forchheimer's Correction

In its classical formulation, Darcy's law is obtained under the hypothesis that $\boldsymbol{\pi}_{fd}$ is determined through a constitutive function, $\hat{\boldsymbol{\pi}}_{fd}$, of the deformation gradient tensor, \mathbf{F} , and the filtration velocity, \mathbf{q} , with linear dependence on \mathbf{q} , i.e.,

$$\boldsymbol{\pi}_{fd} = \hat{\boldsymbol{\pi}}_{fd}(\mathbf{F}, \mathbf{q}) = -\mathbf{g}^{-1} \hat{\mathbf{r}}(\mathbf{F}) \mathbf{q}, \quad (8)$$

where $\mathbf{r} = \hat{\mathbf{r}}(\mathbf{F}) \in [TS]_2^0$ is the *resistivity tensor*. We assume that \mathbf{r} is symmetric and positive-definite and, thus, also invertible. Hence, by substituting (8) into (7), and solving for \mathbf{q} , we obtain Darcy's law

$$\mathbf{q} \equiv \mathbf{q}_D = -\phi_f \mathbf{r}^{-1} \text{grad } p = -\mathbf{k} \text{grad } p, \quad (9)$$

where $\mathbf{k} = \phi_f \mathbf{r}^{-1} \in [TS]_0^2$ is the *permeability tensor*. In this work, we study the case in which $\hat{\boldsymbol{\pi}}_{fd}$ is a quadratic function of the filtration velocity (i.e., (8) no longer applies), but the simplified momentum balance law (7) is still valid. When these conditions apply, one speaks of Forchheimer's correction to Darcy's law [5]. Following [53], we can express the relation between \mathbf{q}_D and the “corrected” filtration velocity, \mathbf{q} , as (with our notation)

$$(\mathbf{i} + \mathcal{F}) \mathbf{q} = \mathbf{q}_D, \quad (10)$$

where \mathbf{i} is the identity tensor, and the tensor $\mathcal{F} \in [TS]_1^1$ is the “*Forchheimer's correction tensor*” [53]. To obtain (10), Whitaker studied a porous medium subjected to no deformation, and applied the volume-averaging method to the Navier-Stokes equation modelling the pore scale dynamics of the fluid [53]. In his work, the correction tensor \mathcal{F} was determined by solving auxiliary “*closure problems*” under the assumption that, at a sufficiently fine scale, the porous medium enjoys the discrete symmetry of spatial periodicity. Moreover, \mathcal{F} was proven to depend linearly on the norm of the filtration velocity, in the limit of sufficiently small Reynolds numbers [53].

By adapting the theoretical framework of [5] to our problem, we show that Forchheimer's correction (10) can be deduced from the dissipation inequality (6). To accomplish our task, we suppose that the theoretical framework deduced in [53] for non deformable porous media can describe also those tissues undergoing (finite) deformations, even though such deformations can compromise the periodicity of the internal structure. Thus, by relaxing the hypothesis of periodic internal structure, we postulate that the dissipative force $\boldsymbol{\pi}_{fd}$ takes on the form

$$\boldsymbol{\pi}_{fd} = -[\mathbf{i} + \|\mathbf{q}\| \mathcal{A}] \mathbf{g}^{-1} \mathbf{r} \mathbf{q}, \quad (11)$$

where we have set $\mathcal{F} := \|q\|\mathcal{A}$, and refer to $\mathcal{A} \in [TS]_1^1$ as to the *tensorial Forchheimer coefficient*. By substituting (11) into (7), multiplying both sides of the resulting expression by the inverse of the resistivity tensor, \mathbf{r}^{-1} , and invoking the definition of the permeability tensor, $\mathbf{k} = \phi_f \mathbf{r}^{-1}$, we obtain

$$[\mathbf{i} + \|q\|\mathbf{k}\mathfrak{A}\mathbf{k}^{-1}]\mathbf{q} = \mathbf{q}_D, \quad (12)$$

where $\mathfrak{A} := g\mathcal{A}g^{-1}$ is the counterpart of \mathcal{A} in the tensor space $[TS]_1^1$. Our result (12) is consistent with similar results found in the literature (cf. e.g. [52], in which the case of an anisotropic porous medium is considered).

To express the Forchheimer coefficient \mathfrak{A} , we introduce the “associated” permeability tensor $\boldsymbol{\kappa} = g\mathbf{k} \in [TS]_1^1$ and we assume $\mathfrak{A} := \varrho_f \boldsymbol{\kappa} \boldsymbol{\beta}$, where $\boldsymbol{\beta} \in [TS]_1^1$ is called *non-Darcy coefficient tensor* [52], and is defined according to the empirical law $\boldsymbol{\beta} = c_0 \phi_f^{c_1} \mu^{c_2} \boldsymbol{\kappa}^{c_2}$ adapted from [46], in which μ is the viscosity of the fluid, and $c_0 \geq 0$, c_1 , and c_2 are real constants. In the jargon of Thauvin and Mohanty [46], formulae of this type are said to be “*correlations*”, since they express the non-Darcy coefficient in terms of other relevant parameters pertaining to the flow as well as the structure of the considered porous medium. Since c_2 is a real number, the power law $\boldsymbol{\kappa}^{c_2}$ is conveniently written in spectral form as

$$\boldsymbol{\kappa}^{c_2} = \sum_{\alpha=1}^3 (k_\alpha)^{c_2} \mathbf{n}^\alpha \otimes \mathbf{n}_\alpha, \quad (13)$$

where k_α is the α th eigenvalue of the permeability tensor, $\mathbf{n}^\alpha \in T^*\mathcal{S} = [TS]_1^0$ is its corresponding eigencovector (determined by $[\boldsymbol{\kappa} - k_\alpha \mathbf{i}^T]\mathbf{n}^\alpha = \mathbf{0}$), and $\mathbf{n}_\alpha = g^{-1}\mathbf{n}^\alpha$ is the associated eigenvector. By employing (13), the Forchheimer coefficient \mathfrak{A} acquires the expression

$$\begin{aligned} \mathfrak{A} &:= \varrho_f \boldsymbol{\kappa} \boldsymbol{\beta} = c_0 \varrho_f \phi_f^{c_1} \mu^{c_2} \boldsymbol{\kappa} \boldsymbol{\kappa}^{c_2} \\ &= c_0 \varrho_f \phi_f^{c_1} \mu^{c_2} \sum_{\alpha=1}^3 (k_\alpha)^{1+c_2} \mathbf{n}^\alpha \otimes \mathbf{n}_\alpha. \end{aligned} \quad (14)$$

According to (14), the tensors $\boldsymbol{\kappa}$ and $\boldsymbol{\beta}$ are coaxial, and thus commute, i.e., it holds that $\mathfrak{A} = \varrho_f \boldsymbol{\kappa} \boldsymbol{\beta} = \varrho_f \boldsymbol{\beta} \boldsymbol{\kappa}$. This implies

$$\begin{aligned} \mathbf{k}\mathfrak{A}\mathbf{k}^{-1} &= \mathbf{k}(\varrho_f \boldsymbol{\kappa} \boldsymbol{\beta})\mathbf{k}^{-1} = \mathbf{k}(\varrho_f \boldsymbol{\beta} \boldsymbol{\kappa})\mathbf{k}^{-1} \\ &= g^{-1}(\varrho_f \boldsymbol{\kappa} \boldsymbol{\beta})g = g^{-1}\mathfrak{A}g = \mathcal{A}, \end{aligned} \quad (15)$$

and, consequently, the relation (12) becomes

$$[\mathbf{i} + \|q\|\mathcal{A}]\mathbf{q} = \mathbf{q}_D. \quad (16)$$

Finally, with the aid of (14), the identity $\mathcal{A} = g^{-1}\mathfrak{A}g$ leads to

$$\mathcal{A} = c_0 \varrho_f \phi_f^{c_1} \mu^{c_2} \sum_{\alpha=1}^3 (k_\alpha)^{1+c_2} \mathbf{n}_\alpha \otimes \mathbf{n}^\alpha. \quad (17)$$

We remark that introducing the Forchheimer coefficient into (11) is equivalent to defining an effective resistivity tensor, $\mathbf{r}_F := \mathbf{r} + \|q\|\mathfrak{A}\mathbf{r}$. Hence, $\boldsymbol{\pi}_{fd}$ admits the expression $\boldsymbol{\pi}_{fd} = -g^{-1}\mathbf{r}_F \mathbf{q}$, which is formally similar to (8), but accounts for Forchheimer’s correction. Moreover, computing explicitly \mathbf{r}_F , with $\mathbf{r} = \phi_f \mathbf{k}^{-1}$ and \mathfrak{A} given in (14), yields

$$\begin{aligned} \mathbf{r}_F &= \phi_f \mathbf{k}^{-1} \\ &+ c_0 \|q\| \varrho_f \phi_f^{1+c_1} \mu^{c_2} \left(\sum_{\alpha=1}^3 (k_\alpha)^{c_2} \mathbf{n}^\alpha \otimes \mathbf{n}^\alpha \right). \end{aligned} \quad (18)$$

Since the hypothesis of positive-definiteness of \mathbf{k} implies that \mathbf{r}_F is positive-definite too, the dissipation inequality is respected, and can be written in compact form as $\mathfrak{D} = \phi_f^{-1} \mathbf{r}_F : (\mathbf{q} \otimes \mathbf{q}) \geq 0$.

Before going further, we emphasise that the tensorial Forchheimer coefficient \mathcal{A} written in (17) stems from the empirical laws expressing \mathfrak{A} and $\boldsymbol{\beta}$, in which the coefficients c_0 , c_1 , and c_2 are to be determined experimentally. Thauvin and Mohanty [46] studied non-deforming isotropic porous media, for which it holds that $\mathbf{k} = k_0 g^{-1}$, and the non-Darcy coefficient tensor is represented by the scalar quantity $\beta = c_0 \phi_f^{c_1} \mu^{c_2} k_0^{c_2}$. Moreover, they found several expressions for β , each corresponding to a set of scalars $\{c_0, c_1, c_2\}$, obtained for different pore structures and system sizes. Some of the correlations considered in [46] were assumed to depend also on the (scalar) tortuosity of the porous medium. On the contrary, since we are not aware of expressions of $\boldsymbol{\beta}$ explicitly determined for articular cartilage, in the present work we consider $\boldsymbol{\beta}$, by choosing c_0 , c_1 , and c_2 from the literature, with a certain amount of freedom ascribable to the lack of experimental data. The tortuosity is not taken into account in the realisations of the non-Darcy coefficient tensor $\boldsymbol{\beta}$ considered here, since, to the best of our knowledge, there is no experimental evidence of such parameter in articular cartilage.

4 Materials Reinforced by Statistically Oriented Fibres

Following the line of thought and notation in [12], the porous fibre-reinforced composite material studied in this work is assumed to have a statistical distribution of fibres, described by the probability distribution function $\Psi : \mathbb{S}^2 \mathcal{B} \rightarrow \mathbb{R}_0^+$, where $\mathbb{S}^2 \mathcal{B}$ is the collection of all vectors $\mathbf{M}_X \in T_X \mathcal{B}$, with X varying in \mathcal{B} , such that $\|\mathbf{M}_X\| = 1$. The value $\Psi(\mathbf{M}_X)$ represents the probability density that, at a point X , a fibre is locally aligned along \mathbf{M}_X . The probability density satisfies the normalisation condition $\int_{\mathbb{S}^2 \mathcal{B}} \Psi(\mathbf{M}) = 1$ and, since in

this work we restrict our attention to phenomena that involve only the direction of the fibres, but not their sense, we require Ψ to fulfil also the symmetry condition $\Psi(-\mathbf{M}) = \Psi(\mathbf{M})$. We also introduce the notation

$$\langle\langle \mathfrak{F} \rangle\rangle = \int_{\mathbb{S}^2 \mathcal{B}} \Psi(\mathbf{M}) \mathfrak{F}(\mathbf{M}), \quad (19)$$

denoting the *directional average* of the quantity \mathfrak{F} with respect to the probability density Ψ .

The composite is assumed to exhibit hyperelastic behaviour from the reference configuration \mathcal{B} , and its elastic potential is constructed by superimposing the elastic contribution of the matrix to that of the fibres, i.e.,

$$\hat{W}(\mathbf{C}) = \Phi_s \hat{U}(J) + \Phi_{0s} \hat{W}_0(\mathbf{C}) + \Phi_{1s} \hat{W}_e(\mathbf{C}), \quad (20)$$

with $J \equiv J(\mathbf{C}) = \sqrt{\det(\mathbf{C})}$

$$\hat{U}(J) = \mathcal{H}(J_{\text{cr}} - J)(J - J_{\text{cr}})^{2q}(J - \Phi_s)^{-r}, \quad (21a)$$

$$\hat{W}_0(\mathbf{C}) = \alpha_0 \frac{\exp(\alpha_1[I_1 - 3] + \alpha_2[I_2 - 3])}{[I_3]^{\alpha_3}}, \quad (21b)$$

$$\hat{W}_e(\mathbf{C}) = \hat{W}_{1i}(\mathbf{C}) + \langle\langle \hat{W}_{1a}(\mathbf{C}, \mathbf{A}) \rangle\rangle, \quad (21c)$$

$$\hat{W}_{1a}(\mathbf{C}, \mathbf{A}) = \mathcal{H}(I_4 - 1)^{\frac{1}{2}c} [I_4 - 1]^2, \quad (21d)$$

where, for brevity, we used I_1, I_2, I_3 for the three principal invariants $I_1(\mathbf{C}) = \text{tr}(\mathbf{C})$, $I_2(\mathbf{C}) = \frac{1}{2}\{[\text{tr}(\mathbf{C})]^2 - \text{tr}(\mathbf{C}^2)\}$, $I_3(\mathbf{C}) = \det(\mathbf{C})$ of the right Cauchy-Green deformation tensor \mathbf{C} , and I_4 for the fourth invariant $I_4(\mathbf{C}, \mathbf{A}) = \mathbf{C} : \mathbf{A}$ of \mathbf{C} [44], in which $\mathbf{A} = \mathbf{M} \otimes \mathbf{M}$ is the structure tensor field.

The contribution $\hat{U}(J)$ is a penalty term depending solely on J , and accounting for the fact that, after the fluid has flown away and the pores are closed, the tissue behaves as an incompressible material. In (21a), \mathcal{H} is the Heaviside function, $J_{\text{cr}} \in]\Phi_s, 1]$, $q \geq 2$ and $r \in]0, 1]$. The quantity J_{cr} specifies a “critical value” of the volume ratio J , below which the penalty term is active. When this occurs, $\hat{U}(J)$ diverges for $J \rightarrow \Phi_s^+$, thereby preventing the violation of the unilateral constraint $J \geq \Phi_s$. A representation of $\hat{U}(J)$ is in Fig. 1. The elastic potential $\hat{W}_0(\mathbf{C})$ in (21b) describes the hyperelastic response of the matrix alone, which is assumed to be isotropic. The constitutive expression of $\hat{W}_0(\mathbf{C})$ is taken from [26], where the coefficients $\alpha_0, \alpha_1, \alpha_2$, and α_3 are model parameters. In (21c) and (21d), $\hat{W}_{1i}(\mathbf{C})$ denotes the isotropic part of the fibre elastic potential, $\hat{W}_{1a}(\mathbf{C}, \mathbf{A})$ denotes the anisotropic elastic potential depending on the local direction of fibre alignment, c is a material parameter, and the Heaviside step function is introduced to eliminate the contribution of the fibres that are not stretched (i.e., those for which $I_4 \leq 1$).

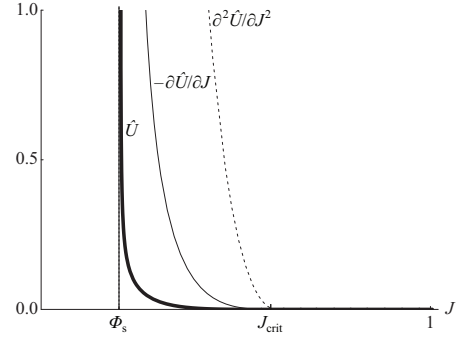


Fig. 1 Graphical representation of the penalty term $\hat{U}(J)$. The vertical asymptote at $J = \Phi_s$ expresses that $\hat{U}(J)$ diverges at compaction, i.e., when the lower bound $J = \Phi_s$ of the admissible values of J is approached. The penalty term is active only for $J < J_{\text{crit}}$, and is zero otherwise. Graphics adapted from [12].

The anisotropic part of $\hat{W}(\mathbf{C})$ generates the anisotropic contribution to $\boldsymbol{\sigma}_{\text{sc}}$ given by

$$\hat{\boldsymbol{\sigma}}_a(\mathbf{F}) = \frac{2\Phi_{1s}}{J} \langle\langle \mathcal{H}(I_4 - 1)c[I_4 - 1]\mathbf{F}\mathbf{A}\mathbf{F}^T \rangle\rangle, \quad (22)$$

where again, for brevity, we used I_4 for $I_4(\mathbf{C}, \mathbf{A})$. To study the material symmetries satisfied by the constitutive tensor function $\hat{\boldsymbol{\sigma}}_a(\mathbf{F})$, we choose arbitrarily $X \in \mathcal{B}$, and consider the group of all proper rotations about a material unit vector \mathbf{M} attached at X , i.e.,

$$\mathcal{G}_X(\mathbf{M}) := \{\mathbf{H} \in \text{Orth}^+ : \mathbf{H}\mathbf{M} = \pm\mathbf{M}\}. \quad (23)$$

Hence, we notice that the integrand of (22) is a transversely isotropic tensor function with respect to \mathbf{M} because, for all $\mathbf{H} \in \mathcal{G}_X(\mathbf{M})$, the structure tensor fulfils the equality $\mathbf{A} = \mathbf{H}\mathbf{A}\mathbf{H}^T$, I_4 is (by definition) invariant under the transformation $\mathbf{F} \mapsto \tilde{\mathbf{F}} = \mathbf{F}\mathbf{H}$, and so is also the tensor $\mathbf{F}\mathbf{A}\mathbf{F}^T$, i.e.,

$$\mathbf{F}\mathbf{A}\mathbf{F}^T \mapsto \tilde{\mathbf{F}}\mathbf{A}\tilde{\mathbf{F}}^T = \mathbf{F}\mathbf{H}\mathbf{A}\mathbf{H}^T\mathbf{F}^T = \mathbf{F}\mathbf{A}\mathbf{F}^T. \quad (24)$$

If there exists a polar axis \mathbf{M}_0 , such that the probability density Ψ is restricted by the symmetry condition

$$\Psi(\mathbf{H}\mathbf{M}) = \Psi(\mathbf{M}), \quad (25)$$

for every $\mathbf{M} \in \mathbb{S}^2 \mathcal{B}$ and for every $\mathbf{H} \in \text{Orth}^+$ such that $\mathbf{H}\mathbf{M}_0 = \pm\mathbf{M}_0$, then Ψ is said to be transversely isotropic with respect to \mathbf{M}_0 and, because of the integration over all possible directions performed in (22), $\hat{\boldsymbol{\sigma}}_a(\mathbf{F})$ is invariant under arbitrary rotations about \mathbf{M}_0 .

Permeability is the material property describing the ability of a fluid to flow through the pore space of a porous medium. In this work, we focus on two permeability models that have been recently conceived to study the coupling between fluid flow and deformation in anisotropic porous media undergoing finite deformations. These models were presented in [1] and [12], and

are hereafter referred to as the “AW-model” and “FG-model”, respectively.

The FG-model [12] extends the results obtained in [15] to the framework of finite deformations, and was employed in [47] to investigate the influence of the fibres’ orientation on the permeability of articular cartilage. In the FG-model, the permeability \mathbf{k} is the result of an upscaling method. More precisely, in [15], at each spatial point $x \in \mathcal{B}_t \subset \mathcal{S}$, a (rectified) fibre is assumed to be locally aligned along the unit vector $\mathbf{m} \in T_x \mathcal{S}$. Then, a REV is attached at x and its size is chosen in such a way that it comprehends only the fibre passing from x and the portion of matrix in which the fibre is embedded. Hence, the permeability of the REV, \mathbf{k}_{REV} , is determined by enforcing a self-consistent method [39] (see [15] for details) under the hypothesis of validity of Darcy’s law at the REV scale and in the limit of vanishing fibre permeability and small fibre volumetric fraction. The result obtained within this approach is then generalised to the case of arbitrary fibre volumetric fractions by adopting differential schemes for composite materials [33, 36], and supposing that the permeability of the matrix has a spherical representation. Thus, the REV permeability determined in [15] reads

$$\mathbf{k}_{\text{REV}} = k_0[1 - \phi_{1s}]^2 \mathbf{g}^{-1} + k_0[1 - \phi_{1s}] \phi_{1s} \mathbf{a}, \quad (26)$$

where

$$\begin{aligned} \mathbf{a} &= \mathbf{m} \otimes \mathbf{m} = \frac{\mathbf{F}\mathbf{M}}{\|\mathbf{F}\mathbf{M}\|} \otimes \frac{\mathbf{F}\mathbf{M}}{\|\mathbf{F}\mathbf{M}\|} \\ &= \frac{1}{I_4(\mathbf{C}, \mathbf{A})} \mathbf{F}\mathbf{A}\mathbf{F}^T, \end{aligned} \quad (27)$$

and $\mathbf{m} = \mathbf{F}\mathbf{M}/\|\mathbf{F}\mathbf{M}\|$. We remark that the contributions of the fibre to the permeability of the REV manifest themselves exclusively through the spatial structure tensor \mathbf{a} and the fibre volumetric fraction ϕ_{1s} . Following the constitutive framework of Holmes and Mow [26], the scalar permeability k_0 is expressed as a constitutive function of the deformation through the volume ratio J , i.e.,

$$\begin{aligned} k_0 &:= \hat{k}_0(J) \\ &= k_{0R} \left[\frac{J - \Phi_s}{1 - \Phi_s} \right]^{\kappa_0} \exp\left(\frac{1}{2} m_0 [J^2 - 1]\right), \end{aligned} \quad (28)$$

where k_{0R} and m_0 are material parameters, k_{0R} is the scalar permeability in the undeformed configuration, and the condition $\lim_{J \rightarrow \Phi_s} \hat{k}(J) = 0$ is respected, since the permeability has to vanish at compaction. By computing \mathbf{k}_{REV} at $X \in \mathcal{B}$, and considering the group $\mathcal{G}_X(\mathbf{M})$ defined in (23), it holds that $\hat{\mathbf{k}}_{\text{REV}}(\mathbf{F}\mathbf{H}, \mathbf{A}) = \hat{\mathbf{k}}_{\text{REV}}(\mathbf{F}, \mathbf{A})$, for all $\mathbf{H} \in \mathcal{G}_X(\mathbf{M})$. Thus, the REV permeability is transversely isotropic with respect to \mathbf{M} .

By exploiting (26), the FG-model obtains the spatial permeability, \mathbf{k} , by integrating \mathbf{k}_{REV} over all possible directions, which results in a constitutive function of the deformation gradient alone [12, 47], i.e.,

$$\begin{aligned} \mathbf{k}_{\text{FG}} &= \hat{\mathbf{k}}_{\text{FG}}(\mathbf{F}) = \langle \hat{\mathbf{k}}_{\text{REV}}(\mathbf{F}, \mathbf{A}) \rangle \\ &= J^{-2} \hat{k}_0(J) [J - \Phi_{1s}]^2 \mathbf{g}^{-1} \\ &\quad + J^{-2} \hat{k}_0(J) [J - \Phi_{1s}] \Phi_{1s} \mathbf{F} \hat{\mathbf{Z}}(\mathbf{C}(\mathbf{F})) \mathbf{F}^T, \end{aligned} \quad (29)$$

where \mathbf{C} in (29) is understood as a function of \mathbf{F} , and we set $\mathbf{Z} = \langle \frac{\mathbf{A}}{I_4(\mathbf{C}, \mathbf{A})} \rangle$.

The backward Piola transformation of (29), i.e., $\mathbf{K}_{\text{FG}} = J \mathbf{F}^{-1} \mathbf{k}_{\text{FG}} \mathbf{F}^{-T}$, produces the material permeability of the FG-model:

$$\begin{aligned} \mathbf{K}_{\text{FG}} &= \hat{\mathbf{K}}_{\text{FG}}(\mathbf{C}) = \frac{\hat{k}_0(J) [J - \Phi_{1s}]^2}{J} \mathbf{C}^{-1} \\ &\quad + \frac{\hat{k}_0(J) [J - \Phi_{1s}] \Phi_{1s}}{J} \hat{\mathbf{Z}}(\mathbf{C}). \end{aligned} \quad (30)$$

The AW-model considers several classes of material symmetries and it supplies for each of those the corresponding permeability tensor. To this purpose, it employs the Representation Theorems for functions valued in the space of symmetric second-order tensors [43, 29]. In the case of transverse isotropy with respect to a direction $\mathbf{M} \in T\mathcal{B}$, the AW-model defines the spatial permeability tensor as

$$\begin{aligned} \mathbf{k}_{\text{AW}} &= k_{0i} \mathbf{g}^{-1} + k_{1t} \mathbf{b} + 2k_{2t} \mathbf{b}^2 \\ &\quad + [k_{1a} - k_{1t}] \mathbf{a} + 2[k_{2a} - k_{2t}] \text{sym}(\mathbf{a}, \mathbf{b}), \end{aligned} \quad (31)$$

where the coefficients k_{0i} , k_{1a} , k_{1t} , k_{2a} , and k_{2t} are, in general, functions of the invariants I_1 , I_2 , I_3 , I_4 , and $I_5 = \mathbf{C}^2 : \mathbf{A}$ [44]. We remark that, while in this work \mathbf{a} is defined by (27), the spatial structure tensor used in [1] is given by $\mathbf{F}\mathbf{A}\mathbf{F}^T$ and is, thus, *not* normalised. Therefore, the coefficients k_{1a} , k_{1t} , k_{2a} , and k_{2t} appearing in (31) must be adjusted accordingly in order for (31) to be consistent with the expression provided in [1].

By comparing (26) and (31), one can see that \mathbf{k}_{REV} is retrieved from \mathbf{k}_{AW} in the limit of vanishing k_{1t} , k_{2t} and k_{2a} , and provided that the identifications

$$k_{0i} := \hat{k}_{0i}(J) \equiv J^{-2} \hat{k}_0(J) [J - \Phi_{1s}]^2, \quad (32a)$$

$$k_{1a} := \hat{k}_{1a}(J) \equiv J^{-2} \hat{k}_0(J) [J - \Phi_{1s}] \Phi_{1s} \quad (32b)$$

are made. In fact, whereas neglecting k_{1t} and k_{2t} can be physically motivated by the observation that the permeability along the fibres is much higher than that across the fibres [47], the absence of a coefficient of the type k_{2a} in the expression of \mathbf{k}_{REV} descends from the chosen upscaling criterion. We regard this feature as a weak point of the FG-model.

From here on, we consider only a “reduced” and slightly modified version of the AW-model, obtained by setting k_{1t} , k_{2t} , and k_{2a} equal to zero, and choosing $k_{0i} = \hat{k}_{0i}(J) \equiv \hat{k}_0(J)$, and $k_{1a} := \hat{k}_{1a}(J) \equiv J^{-2}\hat{k}_0(J)$ (cf. the form of k_{1a} with Equation (39) of [1]). Then, we write the statistical average of the material permeability of the AW-model, $\mathbf{K}_{\text{AW}} = J\mathbf{F}^{-1}\mathbf{k}_{\text{AW}}\mathbf{F}^{-\text{T}}$, as

$$\langle \mathbf{K}_{\text{AW}} \rangle = J\hat{k}_0(J)\mathbf{C}^{-1} + J^{-1}\hat{k}_0(J)\hat{\mathbf{Z}}(\mathbf{C}). \quad (33)$$

The difference between (33) and the permeability that would be obtained by adopting the original model by Ateshian and Weiss [1] is due to the division by I_4 in the definition of the spatial structure tensor \mathbf{a} (cf. (27)). Indeed, if the spatial structure tensor were not normalised, as is the case in [1], the second term on the right-hand-side of (33) would read $J^{-1}\hat{k}_0(J)\langle \mathbf{A} \rangle$.

Notice that, while the FG-model predicts that \mathbf{k}_{REV} depends explicitly both on the fibre’s volumetric fraction and on the fibre’s orientation, \mathbf{k}_{AW} depends on the direction of transverse isotropy, but may be independent on ϕ_{1s} . The dependence of \mathbf{k}_{AW} on ϕ_{1s} , however, can be accounted for by extending the constitutive framework.

5 Benchmark Tests

The model described in the previous sections requires to determine the unknowns $\mathcal{U} = \{\chi, p, \mathbf{q}$ or $\mathbf{Q}\}$ through the solution of the equations

$$\text{Div} \left(-Jp\mathbf{g}^{-1}\mathbf{F}^{-\text{T}} + \mathbf{P}_{\text{sc}} \right) = \mathbf{0}, \quad (34a)$$

$$\dot{J} + \text{Div} \mathbf{Q} = 0, \quad (34b)$$

$$(\mathbf{I} + \|\mathbf{q}\|\mathbf{F}^{-1}\mathbf{A}\mathbf{F})\mathbf{Q} = \mathbf{Q}_{\text{D}}, \quad (34c)$$

in which (34c) is the material form of Forchheimer’s correction. In (34a)–(34c), \mathbf{I} is the identity tensor in $[TB]^1$, $\mathbf{Q}_{\text{D}} = -\mathbf{K} \text{Grad} p$ is the material form of Darcy’s law, where \mathbf{K} is given either by (30) or by (33), depending on whether the FG- or the AW-model is used.

Equations (34a)–(34c) must be equipped with the initial and boundary conditions specifying the type of benchmark problem that has to be solved. To this end, we assume that \mathcal{B} coincides with the configuration of a cylindrical sample at time $t_0 = 0$, regarded as undeformed and unloaded, and we partition the boundary of \mathcal{B} as $\partial\mathcal{B} = \Gamma_{\text{L}} \cup \Gamma_{\text{U}} \cup \Gamma_{\text{B}}$, where Γ_{L} , Γ_{U} , and Γ_{B} represent the lower, upper, and lateral surfaces of $\partial\mathcal{B}$, respectively. As benchmark problems, we consider two unconfined compression tests. In both tests, a cylindrical sample of height $L = 1$ mm and circular cross-section of diameter $D = 3$ mm is inserted between two parallel, impermeable and rigid plates, and compressed along

the direction \mathbf{M}_0 of its geometrical axis. For this purpose, a loading history is imposed to the upper plate, while the lower plate is kept fixed. The two plates remain parallel to each other over the entire duration of the tests. In the following, we consider the Cartesian orthonormal vector bases $\{\mathbf{E}_I\}_{I=1}^3$ and $\{\mathbf{e}_i\}_{i=1}^3$, associated with \mathcal{B} and \mathcal{S} , respectively. We assume $\{\mathbf{E}_I\}_{I=1}^3$ and $\{\mathbf{e}_i\}_{i=1}^3$ to be collinear and choose \mathbf{E}_3 coincident with \mathbf{M}_0 .

In the first test, Γ_{L} is clamped at the lower plate. Thus, the original cylindrical shape of the sample is lost during deformation, although each cross section maintains the polar symmetry with respect to the axis $\mathbf{M}_0 \equiv \mathbf{E}_3$. Accordingly, for all times $t \in]t_0, T_{\text{end}}]$, the boundary conditions read

$$\text{On } \Gamma_{\text{U}}, \quad \begin{cases} \chi^3 = \mathbf{g}, \\ (-\mathbf{K} \text{Grad} p) \cdot \mathbf{N} = 0, \end{cases} \quad (35a)$$

$$\text{On } \Gamma_{\text{B}}, \quad \begin{cases} (-Jp\mathbf{g}^{-1}\mathbf{F}^{-\text{T}} + \mathbf{P}_{\text{sc}}) \cdot \mathbf{N} = \mathbf{0}, \\ p = 0, \end{cases} \quad (35b)$$

$$\text{On } \Gamma_{\text{L}}, \quad \begin{cases} \chi(X, t) - \chi(X, 0) = \mathbf{0}, \\ (-\mathbf{K} \text{Grad} p) \cdot \mathbf{N} = 0, \end{cases} \quad (35c)$$

where \mathbf{N} is the unit vector normal to the surface of the sample, and \mathbf{g} is the loading history

$$\mathbf{g}(t) = \begin{cases} L - \frac{t}{T_{\text{ramp}}}u_{\text{T}}, & \text{for } t \in [0, T_{\text{ramp}}], \\ L - u_{\text{T}}, & \text{for } t \in]T_{\text{ramp}}, T_{\text{end}}]. \end{cases} \quad (36)$$

Here, $u_{\text{T}} = 0.2$ mm is the target displacement and $T_{\text{ramp}} = 20$ s is the final instant of time of the loading ramp. The load (36) is kept up to $T_{\text{end}} = 50$ s.

In the second test, which we call “cylindrical unconfined compression test”, we assume that the cylindrical shape of the sample is preserved by requiring that Γ_{U} and Γ_{L} glide frictionlessly on the plates’ surfaces in axial-symmetric way and that Γ_{B} is a free boundary, although the sample is inhomogeneous [cf. (38a)–(40)]. In fact, the inhomogeneity of the sample in the direction $\mathbf{M}_0 \equiv \mathbf{E}_3$ causes the axial strain and radial displacement to be non-constant with the space variable X^3 . Still, even when we consider an inhomogeneous sample [see Eqs. (38a)–(40)], in our simulations the deformed configurations of the sample deviates only slightly from the cylindrical shape (data not shown). Thus, for the purposes of this work, and in particular for the results reported in section 5.2, we approximate the sample’s deformation with a deformation preserving the cylindrical shape. In this case, the conditions (35a) and (35b) as well as the no-flux condition on Γ_{L} still apply, while the null displacement condition on Γ_{L} has to be replaced by the condition $\chi^3(X, t) = 0$, for all $X \in \Gamma_{\text{L}}$ and for all $t \in]t_0, T_{\text{end}}]$.

With respect to the orthonormal vector basis $\{\mathbf{E}_I\}_{I=1}^3$, \mathbf{M} is written as

$$\begin{aligned}\mathbf{M} &= \hat{\mathbf{M}}(\Theta, \Phi) \\ &= \sin \Theta \cos \Phi \mathbf{E}_1 + \sin \Theta \sin \Phi \mathbf{E}_2 + \cos \Theta \mathbf{E}_3,\end{aligned}\quad (37)$$

where $\Theta \in [0, \pi]$ is the co-latitude and $\Phi \in [0, 2\pi]$ is the longitude, and the transverse isotropy of the probability density Ψ means that there exists a function $\wp : [0, \pi] \rightarrow \mathbb{R}_0^+$ such that the conditions $\Psi(\mathbf{M}) = \Psi(\hat{\mathbf{M}}(\Theta, \Phi)) = \wp(\Theta)$ is verified for all $\Phi \in [0, 2\pi]$. The function \wp must comply with the normalisation condition and with the symmetry condition $\wp(\Theta) = \wp(\pi - \Theta)$, for all $\Theta \in [0, \pi]$, which corresponds to $\Psi(\mathbf{M}) = \Psi(-\mathbf{M})$. Moreover, since in this work we compute the statistical averages of functions that depend on direction only through the structure tensor, we are allowed to restrict the averaging integrals to one hemisphere only (e.g. the “northern” hemisphere $\mathbb{S}^2 + \mathcal{B}$). Hence, we introduce the probability density $\bar{\wp} : [0, \pi/2] \rightarrow \mathbb{R}_0^+$ such that the normalisation reads $2\pi \int_0^{\pi/2} \bar{\wp}(\Theta) \sin(\Theta) d\Theta = 1$. In this work, we use the pseudo-Gaussian distribution [13]

$$\bar{\wp}(\Theta, \xi) = \frac{\mathbf{p}(\Theta, \xi)}{2\pi \int_0^{\pi/2} \mathbf{p}(\Theta', \xi) \sin(\Theta') d\Theta'}, \quad (38a)$$

$$\mathbf{p}(\Theta, \xi) = \exp\left(-\frac{[\Theta - Q(\xi)]^2}{2[\omega(\xi)]^2}\right), \quad (38b)$$

where both the mean angle $Q(\xi)$ and the standard deviation $\omega(\xi)$ depend on the normalised axial coordinate $\xi = X^3/L$, and are given by [13]

$$Q(\xi) = \frac{\pi}{2} \left[1 - \cos\left(\left(-\frac{2}{3}\xi^2 + \frac{5}{3}\xi\right) \frac{\pi}{2}\right) \right], \quad (39a)$$

$$\omega(\xi) = 10^3[(1 - \xi)\xi]^4 + 0.03. \quad (39b)$$

A graphical representation of the functions $\mathbf{p}(\Theta, \xi)$, $Q(\xi)$, and $\omega(\xi)$, defined in (38b), (39a), and (39b), respectively, is reported in Fig. 2. The angle $Q(\xi)$ ranges continuously from $Q(0) = 0$ rad at the lower boundary (cartilage-bone interface) to $Q(1) = \pi/2$ rad at the upper boundary (articular surface). The variance, in turn, is greater in the middle zone, since in that zone the fibres are almost randomly oriented, and thus the tissue could be thought of as isotropic. Hence, the probability density tends to be peaked around 0 rad for ξ approaching zero, and around $\pi/2$ rad, for ξ approaching unity.

The model parameters used for the numerical simulations of the considered benchmark tests are taken from [47]. By employing experimental data available in the literature [24, 10, 2], we provide polynomial expressions for the volumetric fractions, i.e., $\Phi_{0s}(\xi) = -0.062\xi^2 + 0.038\xi + 0.046$, $\Phi_{1s}(\xi) = 0.062\xi^2 - 0.138\xi + 0.204$, and $1 - \Phi_s(\xi) = 0.100\xi^2 + 0.750$. To determine

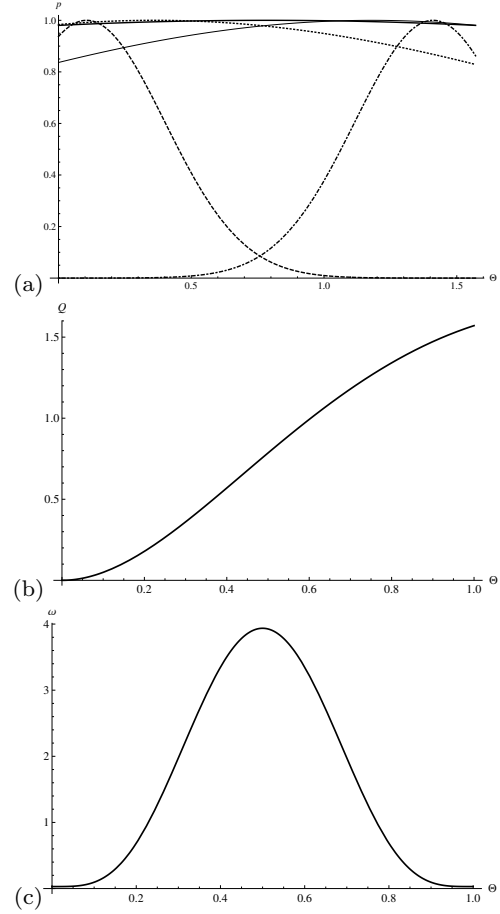


Fig. 2 Graphical representation of (a) the probability density distribution in (38b) as a function of Θ parameterised by ξ (dashed line: $\xi = 0.15$; dotted line: $\xi = 0.30$; thick line: $\xi = 0.50$; thin line: $\xi = 0.70$; dashed-dotted line: $\xi = 0.85$); (b) the histological profile of the mean angle $Q(\xi)$ given in (39a); and (c) the standard deviation $\omega(\xi)$ given in (39b).

K_{FG} and $\langle K_{AW} \rangle$ (cf. (30) and (33), respectively), it is necessary to specify κ_0 , m_0 , and \hat{k}_{0R} . As done in [47], we take here $\kappa_0 = 0.0848$ and $m_0 = 4.638$ [25], and we prescribe k_{0R} to be a function of the normalised axial coordinate [54], i.e.,

$$k_{0R} \equiv k_{0R}(\xi) = k_{0R}^{(0)} \left[\frac{e_R(\xi)}{e_R^{(0)}} \right]^{\kappa_0} \exp\left(\frac{1}{2} m_0 \left[\left(\frac{1+e_R(\xi)}{1+e_R^{(0)}} \right)^2 - 1 \right]\right), \quad (40)$$

where $k_{0R}^{(0)} = 0.003 \text{ mm}^4 \text{ N}^{-1} \text{ s}^{-1}$ is a referential value of the scalar permeability (taken of the same order of magnitude as that reported in [3]), while $e_R(\xi) = (1 - \Phi_s(\xi))/\Phi_s(\xi)$ is the *void ratio* associated with the undeformed configuration (i.e., the ratio between the fluid and the solid volumetric fractions in the undeformed configuration), and $e_R^{(0)} = 4.0$ [34] is a referential value for $e_R(\xi)$. Moreover, we assume $\hat{W}_{1i} = \hat{W}_0$

and, as done in [47], we compute the parameters α_0 , α_1 , and α_2 featuring in (21b) by imposing the condition that the elastic coefficients obtained by linearising $\hat{W}_0(\mathbf{C})$ are identical to those experimentally determined in [3], and fitted to the biphasic indentation model presented in [30]. Since the samples of articular cartilage used for the experiments reported in [3] were intact and comprised both the matrix of proteoglycans and the chondrocytes, we conclude that α_0 , α_1 , and α_2 refer to the mixture of proteoglycans and cartilage cells. For this purpose, we adopt the formulae provided in [26], in which α_0 , α_1 , and α_2 are written as functions of the Lamé's constants. This calculation leads to $\alpha_0 = 0.1250$ MPa, $\alpha_1 = 0.7778$, and $\alpha_2 = 0.1111$. Finally, we choose $c = 7.5$ MPa [47].

Equations (34a)–(34c) are solved numerically by means of Finite Element methods. This necessitates to introduce the weak forms of (34a)–(34c), which are obtained by multiplying each of these equations by the corresponding test function, integrating the resulting expressions over \mathcal{B} , and applying Gauss Theorem, where required, along with the boundary conditions characterising the chosen benchmark tests. Thus, one obtains:

$$\int_{\mathcal{B}} \{\tilde{p}j - (\text{Grad } \tilde{p})\mathbf{Q}\} = 0, \quad (41a)$$

$$\int_{\mathcal{B}} \mathbf{P} : \mathbf{g} \text{Grad } \tilde{\mathbf{u}} = 0, \quad (41b)$$

$$\int_{\mathcal{B}} \{[(\mathbf{I} + \|\mathbf{q}\| \mathbf{F}^{-1} \mathcal{A} \mathbf{F})\mathbf{Q}].\tilde{\mathbf{Q}} - \mathbf{Q}_D.\tilde{\mathbf{Q}}\} = 0, \quad (41c)$$

where \tilde{p} , $\tilde{\mathbf{u}}$, and $\tilde{\mathbf{Q}}$ are test functions, taken in suitable functional spaces, and referred to as virtual pressure, virtual velocity, and virtual (material) filtration velocity, respectively. For the finite element discretisation of the problem, piecewise quadratic Lagrange interpolation functions are used for all the unknowns and the corresponding test functions. Equation (41c) is an algebraic auxiliary equation that has been introduced to compute \mathbf{Q} numerically when its analytical determination is cumbersome (for example, when the Forchheimer coefficient tensor, \mathcal{A} , is not spherical).

To compute the required statistical averages, we employ the Spherical Design Algorithm [19, 11, 9]. Finally, we notice that in (34c) and (41c) $\|\mathbf{q}\|$ can be written as $\|\mathbf{q}\| = J^{-1} \sqrt{\mathbf{C} : (\mathbf{Q} \otimes \mathbf{Q})}$, where the term under square root supplies a further coupling between deformation and the flow direction [16].

5.1 The “Equivalent” Scalar Forchheimer Coefficient

Although the permeabilities predicted by both the FG- and the AW-model are not represented by spherical ten-

sors, we start by defining the *equivalent scalar permeability* [16],

$$k_{\text{eq}} := \sqrt{\frac{1}{3} \text{tr}[\mathbf{k}.\mathbf{k}^T]}, \quad (42)$$

which we employ to construct the equivalent non-Darcy coefficient, $\beta_{\text{eq}} = c_0 \phi_f^{c_1} \mu^{c_2} k_{\text{eq}}^{c_2}$, and the “equivalent” scalar Forchheimer’s correction, \mathcal{A}_{eq} , i.e.,

$$\mathcal{A}_{\text{eq}} := \varrho_f k_{\text{eq}} \beta_{\text{eq}} = c_0 \varrho_f \phi_f^{c_1} \mu^{c_2} k_{\text{eq}}^{1+c_2}, \quad (43)$$

with $c_0 \geq 0$. The factor β_{eq} may depend on c_0 , c_1 , and c_2 in several ways. A review on the subject can be found, for example, in [46, 16].

The equivalent scalar Forchheimer coefficient \mathcal{A}_{eq} is determined to invert (34c) analytically, and to study the simplest case of interaction between the anisotropy of the medium and the nonlinearity of the flow. Indeed, if $\mathcal{A}_{\text{eq}} \mathbf{i}$ is used instead of \mathcal{A} in (16), Forchheimer’s correction becomes

$$[1 + \|\mathbf{q}\| \mathcal{A}_{\text{eq}}] \mathbf{q} = \mathbf{q}_D, \quad (44)$$

which is remnant of the result obtained in [23]. An advantage of working with (44) is that it can be readily solved for \mathbf{q} in spite of the nonlinearity of the product $\|\mathbf{q}\| \mathbf{q}$. Indeed, taking the norm of both sides of (44), and rearranging all terms, the equality (44) can be turned into a quadratic equation in $\|\mathbf{q}\|$ [18, 16] whose only admissible solution is given by

$$\|\mathbf{q}\| = \frac{-1 + \sqrt{1 + 4 \mathcal{A}_{\text{eq}} \|\mathbf{q}_D\|}}{2 \mathcal{A}_{\text{eq}}}. \quad (45)$$

Since (45) expresses $\|\mathbf{q}\|$ as a function of $\|\mathbf{q}_D\|$, we can solve (44) for \mathbf{q} , i.e.,

$$\mathbf{q} = f \mathbf{q}_D, \quad (46a)$$

$$f := \frac{2}{1 + \sqrt{1 + 4 \mathcal{A}_{\text{eq}} \|\mathbf{q}_D\|}}, \quad (46b)$$

where f is referred to as *friction factor*. As shown in [16], f can be understood as a function of the product $\mathcal{A}_{\text{eq}} \|\mathbf{q}_D\|$, and, with a slight abuse of notation, we set $f = f(\mathcal{A}_{\text{eq}} \|\mathbf{q}_D\|)$. In particular, f is such that $f(0) = 1$, $f(\mathcal{A}_{\text{eq}} \|\mathbf{q}_D\|) \sim 1 - \mathcal{A}_{\text{eq}} \|\mathbf{q}_D\|$ for $\mathcal{A}_{\text{eq}} \|\mathbf{q}_D\| \rightarrow 0$, and $f(\mathcal{A}_{\text{eq}} \|\mathbf{q}_D\|) \sim (\mathcal{A}_{\text{eq}} \|\mathbf{q}_D\|)^{-1/2}$ for $\mathcal{A}_{\text{eq}} \|\mathbf{q}_D\| \rightarrow +\infty$. We remark that the definition of f given in (46b) looks much like a result obtained in [23] (cf. Equation (20) in [23]).

If the exponents c_1 and c_2 in (43) are chosen as $c_1 = -11/2$ and $c_2 = -1/2$, $\mathcal{A}_{\text{eq}} \|\mathbf{q}_D\|$ can be expressed as a function of the Reynolds number Re_D [4], i.e.,

$$\mathcal{A}_{\text{eq}} \|\mathbf{q}_D\| = c_0 \phi_f^{-5} \text{Re}_D, \quad (47a)$$

$$\text{Re}_D = \varrho_f \sqrt{\frac{k_{\text{eq}} / \phi_f}{\mu}} \|\mathbf{q}_D\|. \quad (47b)$$

Therefore, by substituting (47a) into (46b), f can be expressed as a function of Re_D and ϕ_f , with $c_0 \geq 0$ being the only tuneable parameter, i.e.,

$$f = \frac{2}{1 + \sqrt{1 + 4c_0\phi_f^{-5}\text{Re}_D}}. \quad (48)$$

We emphasise that, while c_0 is assumed to be constant in this work, f varies in space and time, since so do also ϕ_f and Re_D . Moreover, since the filtration velocity is given by $\mathbf{q} = f\mathbf{q}_D$, and f is determined either by (46b) or by (48), the equations necessary to close the model reduce to (34a) and (34b). Finally, we remark that the definition (47b) of Re_D is slightly different from the one given in [4], in which the characteristic value of $\|\mathbf{q}_D\|$ is divided by the characteristic volumetric fraction of the fluid phase.

Equation (48) implies that the strength of Forchheimer's correction is influenced by c_0 . Indeed, the magnitude of the filtration velocity converges to that predicted by Darcy's law in the limit $c_0 \rightarrow 0$, and tends towards zero for increasing c_0 . This description can be formalised by recognising that, for every $\phi_f^{-5}\text{Re}_D$, f can be written as $f = \hat{f}(c_0)$, and can be thus identified with the value taken at c_0 by the strictly monotonically decreasing function $\hat{f} : [0, +\infty[\rightarrow]0, 1]$. This function is defined by the right-hand-side of (48), and satisfies the conditions $\hat{f}(0) = 1$ and $\lim_{c_0 \rightarrow +\infty} \hat{f}(c_0) = 0$. We notice that, since \hat{f} is continuous and strictly monotonically decreasing over $[0, +\infty[$, it is invertible and its inverse $\hat{f}^{-1} :]0, 1] \rightarrow [0, +\infty[$ is continuous. Since we do not have experimental data for c_0 , we use the invertibility of \hat{f} to determine a prescribed value of c_0 such that f stays within a certain acceptable range. More precisely, in a preliminary test, for which $f = 1$, we calculate $\mathcal{R}_0 = \phi_f^{-5}\text{Re}_D$ at a given point and instant of time, and then, by selecting a *trial* friction factor $f_{\text{trial}} \in]0, 1]$, we obtain the corresponding value of c_0 as $c_0 = \hat{f}^{-1}(f_{\text{trial}})$. By substituting this result into (48), f can be related to f_{trial} :

$$f = \frac{2}{1 + \sqrt{1 + \frac{4-4f_{\text{trial}}}{f_{\text{trial}}^2} \phi_f^{-5}\text{Re}_D \mathcal{R}_0}}. \quad (49)$$

In (49), \mathcal{R}_0 is the value of $\phi_f^{-5}\text{Re}_D$ at a point X_U of the boundary line of Γ_U and at time T_{ramp} . Consistently with the behaviour outlined above, f tends to unity in the limit $f_{\text{trial}} \rightarrow 1$, thereby meaning that the filtration velocity tends to converge to Darcy's solution. Since we expect that Forchheimer's correction is moderate in articular cartilage, we regard only small deviations of the flow from the predictions of Darcy's law as physically admissible. Although this suggests to restrict \hat{f}^{-1} to

values of f_{trial} sufficiently close to unity, for the sake of completeness we consider f_{trial} ranging from 0.1 to 0.9.

In the simulations performed in this work, the Reynolds number associated with Darcy's law ranges between 10^{-8} and 10^{-7} , thereby corresponding to a maximum velocity magnitude of about 10^{-5} m/s (see Fig. 4). This range is often distinctive of a purely Darcian regime [4]. A plausible range of variation for f_{trial} and c_0 could be obtained by means of the comparison between the FG- and the AW-model, as done in the present work. Notice that, for a porous medium with $\phi_f \approx 0.75$, the coefficient c_0 would have approximatively the same order of magnitude as Re_D^{-1} , and decreases with f_{trial} .

It should be noticed that, even though f_{trial} is constant, the friction factor reported in (49) depends on space and time, and may also deviate appreciably from f_{trial} . Furthermore, if evaluated at (X_U, T_{ramp}) , it does not return f_{trial} . Indeed, computing $\phi_f^{-5}\text{Re}_D$ in (X_U, T_{ramp}) by accounting for Forchheimer's correction yields a value \mathcal{R}_1 different from \mathcal{R}_0 , which is instead computed by using Darcy's law only. In fact, as we will see in the following, Forchheimer's correction leads to higher pressures and lower magnitudes of the velocity field in the domain, thereby leading to usually lower Reynolds number. In this respect, the friction factor (49) is "inconsistent". This discrepancy, however, can be reduced by iterating the determination of the friction factor as shown in Algorithm 1.

Algorithm 1 Procedure for determining the friction factor f

```

1: Choose a tolerance  $\text{TOL} > 0$  and  $f_{\text{trial}} \in ]0, 1]$ ;
2: Compute  $\mathcal{R}_0$  by using Darcy's law;
3: Compute  $f_0 = \frac{2}{1 + \sqrt{1 + \frac{4-4f_{\text{trial}}}{f_{\text{trial}}^2} \phi_f^{-5}\text{Re}_D \mathcal{R}_0}}$  [cf. Eq. (49)];
4: if  $|f_0(X_U, T_{\text{ramp}}) - f_{\text{trial}}| < \text{TOL}$  then
5:    $f = f_0$ ;
6: else
7:    $k = 0$ ;
8:   Compute  $\mathcal{R}_{k+1}$  by using  $f_k$ ;
9:   Compute  $f_{k+1} = \frac{2}{1 + \sqrt{1 + \frac{4-4f_{\text{trial}}}{f_{\text{trial}}^2} \phi_f^{-5}\text{Re}_D \mathcal{R}_{k+1}}}$ ;
10:  if  $|f_{k+1}(X_U, T_{\text{ramp}}) - f_{\text{trial}}| < \text{TOL}$  then
11:     $f = f_{k+1}$ 
12:  else
13:     $k = k + 1$ ;
14:    Go to 8;

```

To see how the friction factor varies in space, and to highlight how its spatial distribution is influenced by the fluid filtration velocity, which, in turn, depends through the permeability tensor on the anisotropy and inhomogeneity of the tissue, we run two simulations of the first benchmark problem (i.e., an unconfined compression test in which the lower boundary of the sample is clamped). For the first simulation, we consider the

transversely isotropic and inhomogeneous model discussed in the previous sections, while for the second simulation we study a simplified framework in which the anisotropic contribution of the fibres is not taken into account, and all material parameters are constant with the depth of the sample. In particular, we set $\Phi_s = \Phi_{0s} = 0.15$. Hence, the scalar permeability in (40) becomes constant through the depth of the sample, and equal to $k_{0R} = 0.0188 \text{ mm}^4 \text{ N}^{-1} \text{ s}^{-1}$.

By comparing Fig. 3 with Fig. 4, which represent f and \mathbf{q}_D at $t = T_{\text{ramp}}$, respectively, we notice that, as expected, the friction factor is higher in the zones of the sample in which the Reynolds number is lower, i.e., in the central zone of the sample, and it approaches f_{trial} in the external zone, for both the inhomogeneous (Fig. 3(a) and Fig. 4(a)) and the homogeneous case (Fig. 3(b) and Fig. 4(b)). As experimentally observed, both the porosity and the permeability of articular cartilage experience strong variations along the tissue's depth. If the inhomogeneity of these physical quantities is modelled, the pathways of the fluid inside the tissue vary sensibly with respect to the homogeneous case. On the contrary, as shown in Fig. 3(b) and Fig. 4(b), when Φ_s and k_{0R} are assumed to be constant, the variation of both the filtration velocity and the friction factor along the sample depth is less pronounced than it is in the inhomogeneous (and transversely isotropic) case.

We report in Fig. 5 the patterns of \mathbf{q} at $t = T_{\text{ramp}}$, as obtained by employing Forchheimer's correction with $f_{\text{trial}} = 0.1$, both in the inhomogeneous and anisotropic case (Fig. 5a) and in the homogeneous and isotropic case (Fig. 5b). We observe that, when Forchheimer's correction is introduced, the filtration velocity tends to become more spatially uniform than that predicted by Darcy's law, and a small distortion of the streamlines occurs at the bottom of the sample, where zero-displacement boundary conditions are imposed.

In Fig. 6 we show the influence of Forchheimer's correction on the magnitude of the filtration velocity and pressure for different values of f_{trial} . At each time, the values on the vertical axis refer to the maxima attained by the magnitude of the filtration velocity, $\|\mathbf{q}\|$, and pressure, p , within the sample. In particular, $\|\mathbf{q}\|$ is evaluated at the point X_U defined above, while p is taken at the point $X_L = (0, 0, 0)$ (centre of the lower boundary of the sample). First, we report the results of two simulations, performed by using Darcy's law, in which the permeability is given once by the FG-model and once by AW-model. Looking at Fig. 6, we notice that the results predicted by the Darcy-based FG- and AW-model are in remarkable disagreement with each other, although they both seem to be physically plausible. In particular, the AW-model returns a higher filtration velocity

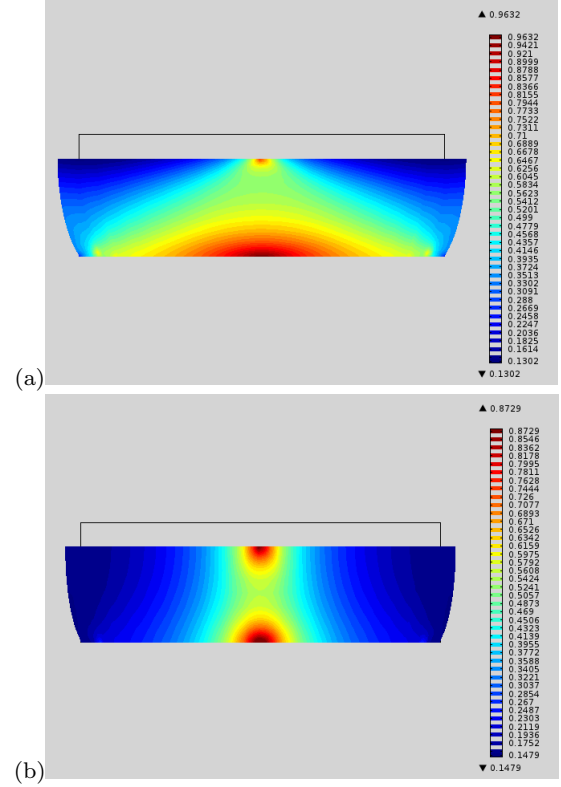


Fig. 3 The friction factor f varies according to the variation of both the filtration velocity and the permeability (computed here with the AW-model). (a): Transversely isotropic and inhomogeneous model with $f_{\text{trial}} = 0.3$. (b): Homogeneous and isotropic case with $f_{\text{trial}} = 0.3$. Close to the outer wall of the sample, where the filtration velocity is higher, the values of f are smaller (thereby yielding a stronger Forchheimer's correction) than those at the centre of the sample. The plots are evaluated at $t = T_{\text{ramp}}$. (Colour figure online)

and a lower pore pressure (black dotted curve) than those obtained by using the FG-model (black curves). By tuning f_{trial} , a partial agreement between the two models can be achieved. Indeed, as we can see from Fig. 6, Forchheimer's correction contributes to lower the magnitude of the filtration velocity and to raise the pressure, thereby reducing the mean distance between the results of the AW-model and those of the FG-model. Moreover, an *optimal* value of f_{trial} can be obtained by means of an optimisation procedure that minimises the distance between the magnitude of Darcy's velocity obtained by means of the FG-model, and the magnitude of the filtration velocity obtained with the AW-model modified by Forchheimer's correction. Here, we set

$$f_{\text{trial}} = f_{\text{opt}} = \tilde{f}_{\text{trial}}(\xi) = 2.38\xi^3 - 3.51\xi^2 + 1.69\xi + 0.07. \quad (50)$$

Such optimal value varies in space, due to the spatial variations of the computed f (see Fig. 3).

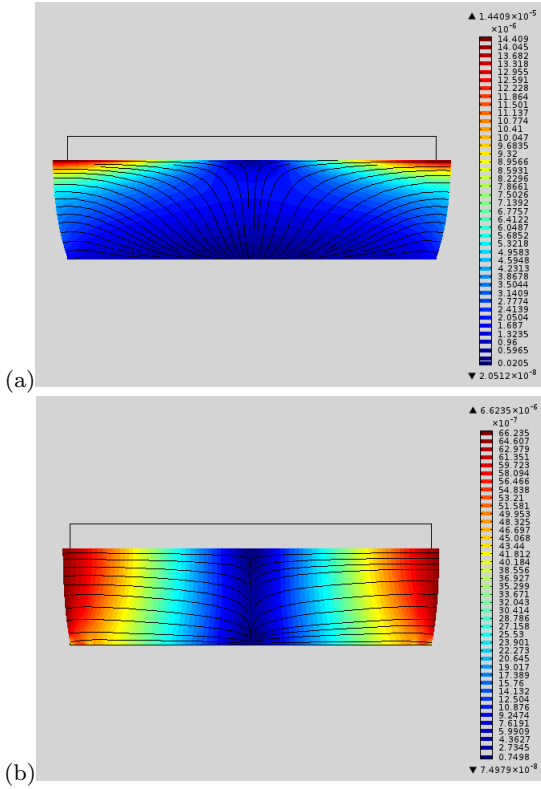


Fig. 4 Patterns of Darcy's filtration velocity \mathbf{q}_D at $t = T_{\text{ramp}}$ as predicted by the AW-model. (a): Transversely isotropic and inhomogeneous model. (b): Isotropic and homogeneous model. The black curves represent the streamlines. The zones of higher velocity correspond to the zones of lower friction factor in Fig. 3. (Colour figure online)

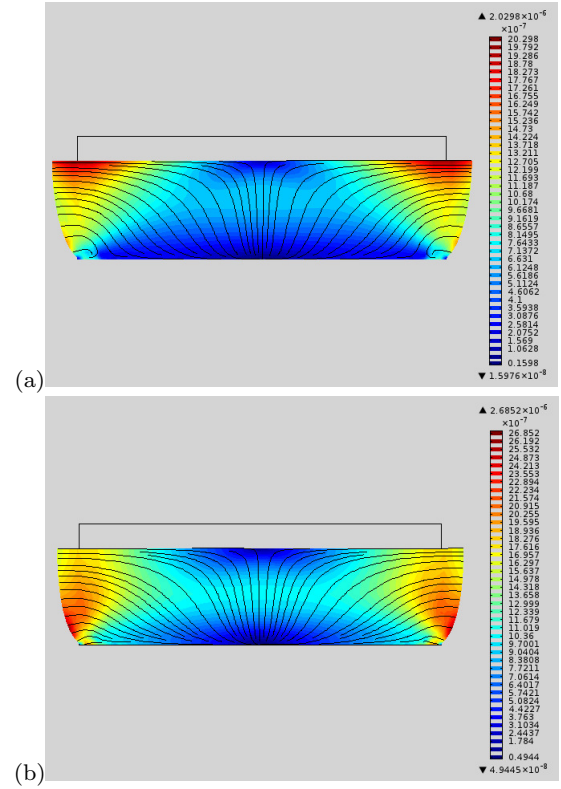


Fig. 5 Patterns of filtration velocity \mathbf{q} at $t = T_{\text{ramp}}$ for $f_{\text{trial}} = 0.1$. (a): Transversely isotropic and inhomogeneous model. (b): Isotropic and homogenous case. The black curves represent the streamlines. Both simulations are obtained for the AW-model. The filtration velocity is more uniform in the domain, and lower than that obtained in the Darcian case (cf. Fig. 4). (Colour figure online)

It is important to notice that, when Forchheimer's correction is introduced, both the magnitude of the filtration velocity and the pressure relax towards the stationary states more slowly than in the Darcian case.

5.2 Diagonal Forchheimer Coefficient Tensor

In this section, we consider the benchmark test of the second kind, in which the original shape of the sample is approximately maintained by the deformation. We say “approximately” because, in spite of tissue's inhomogeneity, the deformed shape of the sample deviates only slightly from the original, cylindrical one. We denote by $\{\mathbf{E}_I(X)\}_{I=1}^3 \in T_X \mathcal{B}$ and $\{\mathbf{e}_i(x)\}_{i=1}^3 \in T_x \mathcal{S}$ the collinear, orthonormal vector bases attached at $X \in \mathcal{B}$ and $x = \chi(X, t) \in \mathcal{S}$, respectively, with $\mathbf{E}_1(X)$ and $\mathbf{e}_1(x)$ oriented radially, $\mathbf{E}_2(X)$ and $\mathbf{e}_2(x)$ circumferentially, and $\mathbf{E}_3(X)$ and $\mathbf{e}_3(x)$ axially. Forchheimer's correction tensor \mathcal{A} is diagonal with respect to the basis

$\{\mathbf{e}_i(x)\}_{i=1}^3 \in T_x \mathcal{S}$, and can be written as

$$\mathcal{A} = \sum_{i=1}^3 \mathcal{A}_i \mathbf{e}_i \otimes \mathbf{e}_i = \sum_{i=1}^3 \mathcal{A}_i \mathbf{e}_i \otimes \mathbf{e}_i, \quad (51)$$

where $\{\mathbf{e}^i(x)\}_{i=1}^3 \in T_x^* \mathcal{S}$ is the covector basis dual of $\{\mathbf{e}_i(x)\}_{i=1}^3 \in T_x \mathcal{S}$, and $\mathcal{A}_i \equiv \mathcal{A}^i_i > 0$, $i \in \{1, 2, 3\}$ (no sum with respect to i), are the transversal and axial components of \mathcal{A} , respectively. Equation (51) permits to rewrite (16) as

$$\left[\sum_{i=1}^3 (1 + \mathcal{A}_i \|\mathbf{q}\|) \mathbf{e}_i \otimes \mathbf{e}_i \right] \mathbf{q} = \mathbf{q}_D. \quad (52)$$

Let $\mathcal{A}_M = \max_{i \in \{1, 2, 3\}} \{\mathcal{A}_i\}$ and $\mathcal{A}_m = \min_{i \in \{1, 2, 3\}} \{\mathcal{A}_i\}$ be the maximum and the minimum eigenvalue of \mathcal{A} , respectively. Hence, the inequality $\mathcal{A}_M \geq \mathcal{A}_m$, with the equality sign being satisfied in the isotropic case, implies the estimates

$$(1 + \mathcal{A}_m \|\mathbf{q}\|) \|\mathbf{q}\| \leq \|\mathbf{q}_D\| \leq (1 + \mathcal{A}_M \|\mathbf{q}\|) \|\mathbf{q}\|. \quad (53)$$

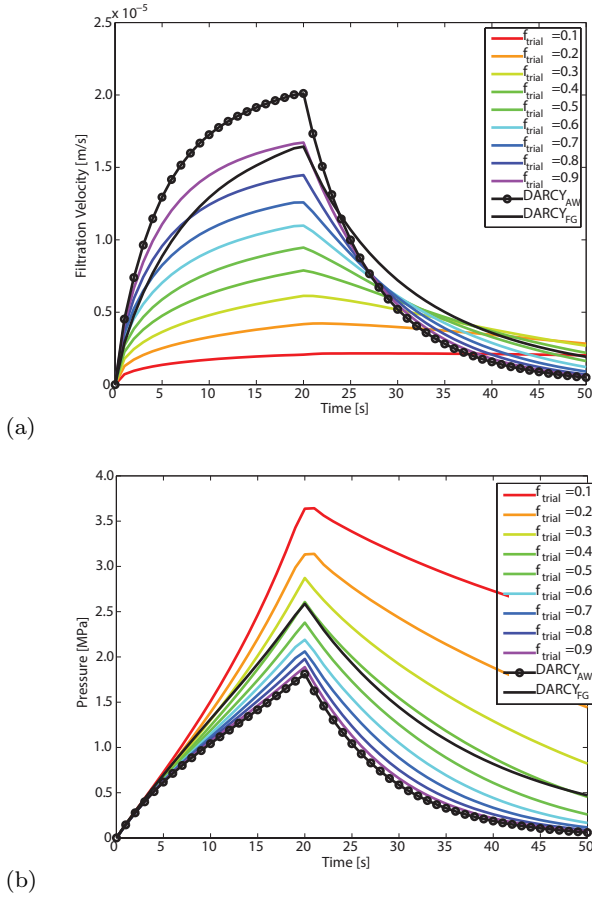


Fig. 6 Magnitude of the filtration velocity $\|\mathbf{q}\|$ (a) and pressure p (b), for different values of f_{trial} , computed at the point of the sample in which each of these quantities attains its maximum. The black solid curves with and without markers represent the output of the AW and the FG model, respectively, in a purely Darcian regime. The coloured curves are obtained by means of the scalar Forchheimer's correction applied to the AW permeability model. (Colour figure online)

By equating $\|\mathbf{q}_D\|$ with its lower and upper bound, Eq. (53) allows to deduce two admissible extremal solutions for $\|\mathbf{q}\|$, i.e.,

$$\gamma(\mathcal{A}_M) := \frac{-1 + \sqrt{1 + 4\mathcal{A}_M\|\mathbf{q}_D\|}}{2\mathcal{A}_M}, \quad (54a)$$

$$\gamma(\mathcal{A}_m) := \frac{-1 + \sqrt{1 + 4\mathcal{A}_m\|\mathbf{q}_D\|}}{2\mathcal{A}_m}. \quad (54b)$$

It can be proven that the inequality $\gamma(\mathcal{A}_M) \leq \gamma(\mathcal{A}_m)$ holds true. Consistently, the magnitude of the filtration velocity is said to be admissible if it complies with the chain of inequalities

$$\gamma(\mathcal{A}_M) \leq \|\mathbf{q}\| \leq \gamma(\mathcal{A}_m). \quad (55)$$

We remark that $\gamma(\mathcal{A}_M)$ and $\gamma(\mathcal{A}_m)$ depend on $\|\mathbf{q}_D\|$, which, in turn, depends on the permeability and pressure gradient. The lower and the upper bounds of $\|\mathbf{q}\|$

are obtained by evaluating the same function, γ , once in the maximum and once in the minimum eigenvalue of \mathcal{A} . Thus, if we set $\|\mathbf{q}\| = \gamma(\mathcal{A}_j)$, with $j \in \{1, 2, 3\}$, and substitute the result into (52), we obtain

$$\begin{aligned} 1 + \mathcal{A}_i\|\mathbf{q}\| &= 1 + \mathcal{A}_i\gamma(\mathcal{A}_j) \\ &= \frac{(2 - \zeta_{ij}) + \zeta_{ij}\sqrt{1 + 4\mathcal{A}_j\|\mathbf{q}_D\|}}{2} \\ &=: \frac{1}{f_{ij}}, \end{aligned} \quad (56)$$

where $\zeta_{ij} := \mathcal{A}_i/\mathcal{A}_j$ is referred to as *anisotropy ratio*, and f_{ij} is said to be the corresponding *friction factor*. Note that $\zeta_{ji} = 1/\zeta_{ij}$, and (52) becomes

$$\left[\sum_{i=1}^3 \frac{1}{f_{ij}} \mathbf{e}_i \otimes \mathbf{e}^i \right] \mathbf{q} = \mathbf{q}_D, \quad j \in \{1, 2, 3\}, \quad (57)$$

which can be inverted to express the filtration velocity as

$$\mathbf{q}_{(j)} = \left[\sum_{i=1}^3 f_{ij} \mathbf{e}_i \otimes \mathbf{e}^i \right] \mathbf{q}_D, \quad j \in \{1, 2, 3\}. \quad (58)$$

where $\mathbf{q}_{(j)}$ is the value of the filtration velocity whose norm is $\gamma(\mathcal{A}_j)$, with $j \in \{1, 2, 3\}$. To complete the description, we provide an explicit expression for the anisotropy factors, ζ_{ij} , with $i, j \in \{1, 2, 3\}$. In the AW-model, the spatial permeability tensor is given by $\mathbf{k} = \mathbf{J}^{-1} \mathbf{F} \langle \mathbf{K}_{AW} \rangle \mathbf{F}^T$, and depends on the tensor \mathbf{Z} . Due to the particular form of the deformation, \mathbf{Z} possesses transverse isotropy with respect to \mathbf{E}_3 , which is parallel to \mathbf{M}_0 . Since $\mathbf{A}_0 := \mathbf{E}_3 \otimes \mathbf{E}_3$ and $\mathbf{T}_0 = \mathbf{E}_1 \otimes \mathbf{E}_1 + \mathbf{E}_2 \otimes \mathbf{E}_2$ span the space of all symmetric second-order tensors of the type $[\mathcal{TB}]_0^2$ exhibiting transverse isotropy with respect to $\mathbf{M}_0 \equiv \mathbf{E}_3$, we can write

$$\mathbf{Z} = \left\langle \frac{\mathbf{A}}{I_4(\mathbf{C}, \mathbf{A})} \right\rangle = Z_t \mathbf{T}_0 + Z_a \mathbf{A}_0, \quad (59)$$

with Z_t and Z_a being the transverse and axial components of \mathbf{Z} , respectively. Since, for the considered benchmark test, \mathbf{F} is assumed to admit in cylindrical coordinates the representation $\mathbf{F} = \lambda_1 \mathbf{e}_1 \otimes \mathbf{E}^1 + \lambda_2 \mathbf{e}_2 \otimes \mathbf{E}^2 + \lambda_3 \mathbf{e}_3 \otimes \mathbf{E}^3$, the tensor $\mathbf{z} = \mathbf{F} \mathbf{Z} \mathbf{F}^T$ is given by

$$\begin{aligned} \mathbf{z} &= Z_t \mathbf{b} + (Z_a - Z_t) \mathbf{F} \mathbf{A}_0 \mathbf{F}^T \\ &= Z_t \mathbf{b} + (Z_a - Z_t) I_{40} \mathbf{a}_0, \end{aligned} \quad (60)$$

with $\mathbf{b} = \sum_{i=1}^3 \lambda_i^2 \mathbf{e}_i \otimes \mathbf{e}_i$ being the left Cauchy-Green deformation tensor, $I_{40} = \mathbf{C} : \mathbf{A}_0 = \lambda_3^2$, and $\mathbf{a}_0 = \mathbf{e}_3 \otimes \mathbf{e}_3$. We remark that \mathbf{Z} features the nonzero transversal component Z_t even though $I_4^{-1} \mathbf{A}$ does not have any

transverse component along the local transverse projection tensor $\mathbf{T} = \mathbf{G}^{-1} - \mathbf{A}$ [50, 51, 47]. Consequently, the spatial permeability is given by

$$\mathbf{k} = \hat{k}_0(J) \mathbf{g}^{-1} + J^{-2} \hat{k}_0(J) Z_t \mathbf{b} + J^{-2} \hat{k}_0(J) (Z_a - Z_t) I_{40} \mathbf{a}_0, \quad (61)$$

and, more explicitly, it can be written as $\mathbf{k} = \sum_{i=1}^3 k_i \mathbf{e}_i \otimes \mathbf{e}_i$, where the scalar permeabilities are defined by

$$k_1 = \hat{k}_0(J) + J^{-2} \hat{k}_0(J) Z_t \lambda_1^2, \quad (62a)$$

$$k_2 = \hat{k}_0(J) + J^{-2} \hat{k}_0(J) Z_t \lambda_2^2, \quad (62b)$$

$$k_3 = \hat{k}_0(J) + J^{-2} \hat{k}_0(J) Z_a \lambda_3^2. \quad (62c)$$

Accordingly, the eigenvalues of the Forchheimer coefficient tensor read

$$\mathcal{A}_1 = c_0 \varrho_f \phi_f^{c_1} \mu^{c_2} \left(\hat{k}_0(J) + J^{-2} \hat{k}_0(J) Z_t \lambda_1^2 \right)^{1+c_2}, \quad (63a)$$

$$\mathcal{A}_2 = c_0 \varrho_f \phi_f^{c_1} \mu^{c_2} \left(\hat{k}_0(J) + J^{-2} \hat{k}_0(J) Z_t \lambda_2^2 \right)^{1+c_2}, \quad (63b)$$

$$\mathcal{A}_3 = c_0 \varrho_f \phi_f^{c_1} \mu^{c_2} \left(\hat{k}_0(J) + J^{-2} \hat{k}_0(J) Z_a \lambda_3^2 \right)^{1+c_2}. \quad (63c)$$

Therefore, if we choose the anisotropy factors ζ_{31} and ζ_{32} , we obtain

$$\zeta_{3j} = \left[\frac{J^2 + Z_a \lambda_3^2}{J^2 + Z_t \lambda_j^2} \right]^{1+c_2}, \quad j = \{1, 2\}. \quad (64)$$

In the undeformed configuration, it holds that $Z_a + 2Z_t = 1$, which yields

$$\zeta_{31} = \zeta_{32} = \zeta = \left[\frac{1 + Z_a}{1 + Z_t} \right]^{1+c_2} = \left[\frac{2 - 2Z_t}{1 + Z_t} \right]^{1+c_2}. \quad (65)$$

Note that, in the undeformed configuration, it holds that $\zeta_{12} = \zeta_{21} = 1$. The correlations used in this work to express β_{eq} were taken from [28], and are referred to as Coles&Hartman correlation, $\beta_{\text{eq}} = c_0 \phi_f^{0.449} \mu^{-1.88} k_{\text{eq}}^{-1.88}$, and Geertsma correlation, $\beta_{\text{eq}} = c_0 \phi_f^{-5.5} \mu^{-0.5} k_{\text{eq}}^{-0.5}$. For the computations, the Coles&Hartman correlation has been approximated by setting $c_2 = -2$.

The curves in Fig. 7a refer to two different sets of computations of the magnitude of the filtration velocity: once by employing the equivalent scalar Forchheimer's coefficient \mathcal{A}_{eq} defined in (43) and the optimised friction factor f_{opt} , and once in the case of diagonal \mathcal{A} . The continuous curve is obtained for $\|\mathbf{q}\| = \gamma(\mathcal{A}_1)$, and the marked curve is obtained for $\|\mathbf{q}\| = \gamma(\mathcal{A}_3)$. From Fig. 7a, we can see that the curve obtained by expressing the norm $\|\mathbf{q}\|$ of the filtration velocity as a function of \mathcal{A}_1 is quite compatible with the one obtained as a result of the equivalent scalar case. The greatest distance between the two curves, i.e., the one obtained for $\|\mathbf{q}\| \equiv \gamma(\mathcal{A}_1)$ and the one obtained

for $\|\mathbf{q}\| \equiv \gamma(\mathcal{A}_3)$, can be registered in the neighbourhood of $t = T_{\text{ramp}}$, i.e., when Forchheimer's correction is more significant due to the higher values of the filtration velocity in the sample. In Fig. 7b, the friction factors f_{ij} , with $i, j = 1, 3$, are compared with f_{opt} . As a consequence of the inhomogeneity of the permeability through the depth of the sample, \mathcal{A}_1 and \mathcal{A}_3 acquire the role of maximum or minimum eigenvalue of \mathcal{A} , respectively. In particular, the axial friction factors f_{13} and f_{33} are higher than the longitudinal ones in the deep zone of the sample. Due to the randomness of the distribution of the fibres in the middle zone, also the material parameters are such that, in this zone, an isotropic behaviour can be observed. In this zone, indeed, all the friction factors merge, whereas at the top of the sample, the transversal friction factors f_{11} and f_{31} have a greater value than the axial ones. Moreover, at the top of the sample, the friction factors related to the transversal eigenvalue \mathcal{A}_1 , i.e., f_{11} and f_{13} , are both higher than the ones related to the axial eigenvalue \mathcal{A}_3 , i.e., f_{31} and f_{33} , whereas the latter two are higher than the transversal ones at the bottom.

5.3 Fully Tensorial Case

In this section, we simulate the second benchmark test, in which the original cylindrical shape of the sample is disrupted by the deformation, and we consider a not necessarily diagonal Forchheimer coefficient \mathcal{A} . In this case, which we call “fully tensorial case”, we prefer to invert the relation (34c) numerically. For determining \mathcal{A} , we employ the non-Darcy coefficient tensor β , with the exponents c_0 , c_1 , and c_2 predicted by the previously introduced approximation of the Coles&Hartman correlation. For comparison, we consider also the benchmark test of the first type (which approximately maintains the sample's cylindrical shape). In Fig. 8, we show the time variation of the magnitude of the filtration velocity, $\|\mathbf{q}\|$, for the fully tensorial case, and for the extremal values $\|\mathbf{q}\| = \gamma(\mathcal{A}_1)$ and $\|\mathbf{q}\| = \gamma(\mathcal{A}_3)$, obtained in the case of diagonal Forchheimer coefficient tensor. From Fig. 8, we see that the Coles&Hartman correlation induces a greater difference between the extremal curves, with respect to those plotted in Fig. 7, which were obtained for c_1 and c_2 taken from the Geertsma correlation, and $c_0 = \hat{f}^{-1}(f_{\text{opt}})$, with $f_{\text{opt}} = \hat{f}_{\text{trial}}(\xi)$ as in (50).

Figure 8 represents also a validation of the results obtained by solving numerically (34c). Indeed, the numerical results of the two extremal cases, $\|\mathbf{q}\| = \gamma(\mathcal{A}_1)$ and $\|\mathbf{q}\| = \gamma(\mathcal{A}_3)$, act as an upper and a lower bound for the results of the fully tensorial case, depending on which eigenvalue attains the maximum and minimum

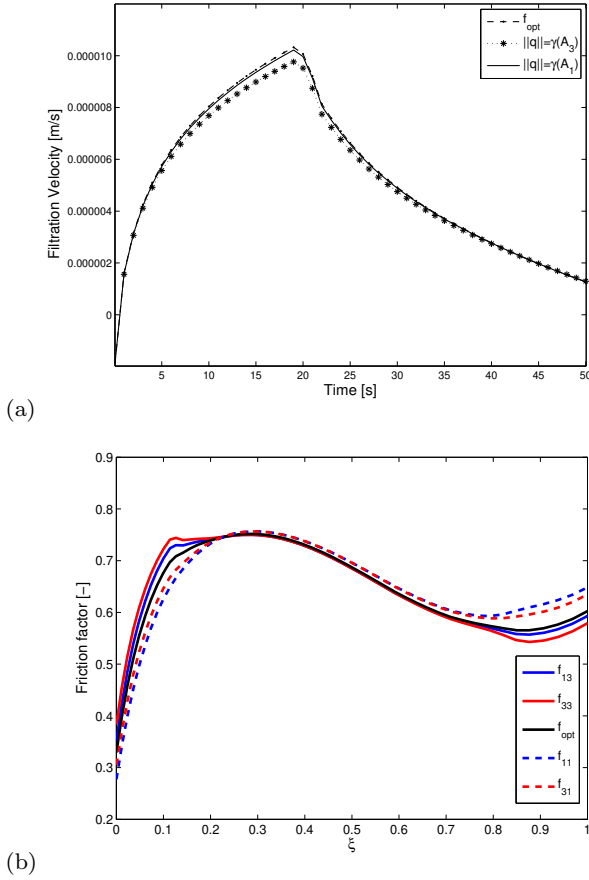


Fig. 7 (a): Filtration velocity evaluated at the upper external point of the sample. (b): Friction factors related to each of them for $t = T_{\text{ramp}}$ vs the normalised axial coordinate ξ . The vertical line along which the variation of the friction factor is observed intersects the lower boundary at $X^1 = X^2 = 0.5$ mm. The blue curves are obtained by means of the formula (56), with $i = 1$ and $j = 1$, for the dashed curve, and $j = 3$, for the solid curve. Analogously, the red curves are obtained by choosing $i = 3$. (Colour figure online)

value, respectively. Thus, in Fig. 7a, we see that the magnitude of the filtration velocity obtained as an outcome of the fully tensorial case lies in between the two extremal solutions, and it is quite compatible with the result obtained with the equivalent scalar Forchheimer's correction.

In Fig. 9a, the results obtained with the scalar Forchheimer's correction, which corresponds here to the optimised friction factor, f_{opt} , are compared with those obtained with the fully tensorial correction for the case of clamped lower boundary of the sample (this boundary condition is closer to the system's phenomenology, since it simulates the attachment of articular cartilage to the subchondral bone). For completeness, we report also the magnitude of the filtration velocity as predicted by the FG- and the AW-model within the Darcian regime.

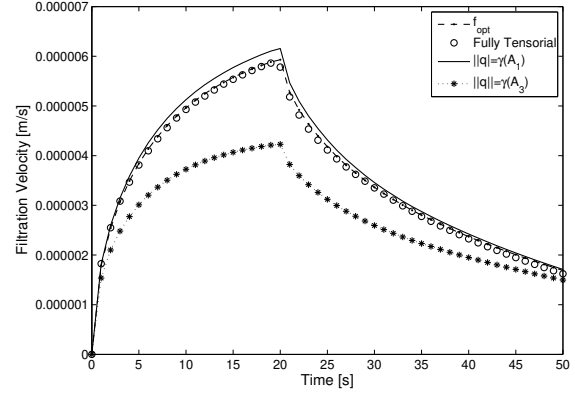


Fig. 8 Magnitude of the filtration velocity for the fully tensorial case (plain rings), for the diagonal case and extremal values $\|q\| = \gamma(A_1)$ and $\|q\| = \gamma(A_3)$ (continuous line and asterisks, respectively), and for the equivalent scalar case with optimised friction factor f_{opt} . All velocities are evaluated at a point X_U of the boundary line of I_U by employing the Coles&Hartman correlation, with $c_0 = 5 \cdot 10^{-18}$.

As seen in Fig. 7a, also with a different boundary condition, the equivalent scalar Forchheimer coefficient and the fully tensorial Forchheimer coefficient return, in our work, a quite compatible numerical result. Indeed, the curves representing the fully tensorial case (plain circles in Fig. 9a) are almost overlapped to the dashed ones, which represent the scalar equivalent case. Finally, Fig. 9b shows the time variation of the pressure at the centre of the lower boundary of the sample. We remark that, in contrast to what happens to the magnitude of the filtration velocity, the pressure predicted by the fully tensorial model is lower than that obtained by the equivalent scalar model. Moreover, the curves obtained within the Darcian regime by employing the FG- and the AW-model predict sufficiently smaller values of pressure and, in particular, the lowest pressures are those predicted by the AW-model. Finally, we notice that, also in the tensorial case, Forchheimer's correction implies that the magnitude of the filtration velocity and pressure relax towards the stationary states more slowly than in the Darcian case.

6 Discussion and Conclusions

In this work, we studied some consequences of Forchheimer's correction to Darcy's law in the study of the fluid flow in a hydrated biological tissue such as articular cartilage. To imitate the internal structure of the examined target tissue, its reinforcing fibres were assumed to be oriented statistically, as predicted by a probability density compatible with the tissue's histology. Also the volumetric fractions of matrix and fibres

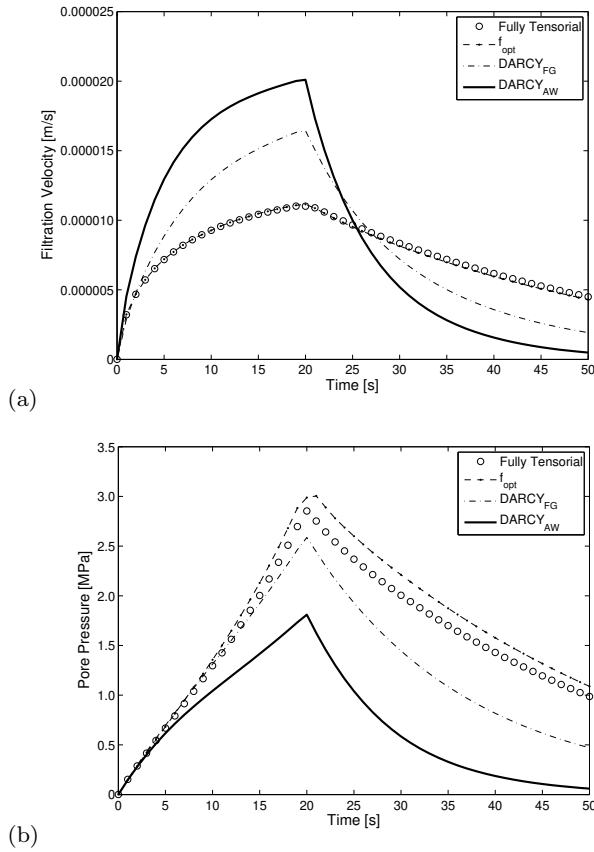


Fig. 9 (a): Magnitude of the filtration velocity for the fully tensorial case (plain rings), for the equivalent scalar case with optimised friction factor f_{opt} (asterisks), for the Darcian regime and FG-model (dash-dotted line), and for the Darcian regime and AW-model (continuous line). All velocities are evaluated at a point X_U of the boundary line of Γ_U , for the Coles&Hartman correlation, with $c_0 = 5 \cdot 10^{-18}$. (b): Pore pressure versus time (curves as in point (a)). Pressures are evaluated at $X_L = (0, 0, 0)$ for the Coles&Hartman correlation, with $c_0 = 5 \cdot 10^{-18}$.

were deduced from experimental data taken from the literature. The mechanical response of the solid matrix of the sample was hypothesised to be hyperelastic, and characterised by the elastic potential defined in (20). Moreover, to study the flow of the interstitial fluid, the FG-model [12] and the AW-model [1] of permeability were compared.

We developed the theory of Forchheimer’s correction for the case of a tensorial Forchheimer’s coefficient. However, in order to adapt our study to well-established derivations of Forchheimer’s correction available in the literature [46], we first introduced an “equivalent” scalar coefficient, \mathcal{A}_{eq} , and the friction factor, f . We observed that the inhomogeneity and anisotropy of the sample yield patterns of f and \mathbf{q}_D that are different from those obtained in the isotropic and homogeneous case, and produce an increase of the maximum value of both f

and $\|\mathbf{q}_D\|$ (see Figs. 3 and 4). The increase of $\|\mathbf{q}_D\|$ might be ascribable to microstructural effects. By introducing Forchheimer’s correction, we obtained a reduction of the magnitude of the filtration velocity (see Fig. 5) with respect to the Darcian description. Moreover, a redistribution of the flow pattern, which tends to become spatially uniform, can be observed. By comparing Figs. 4 and 5, we can also observe that, by applying the same trial friction factor $f_{trial} = 0.1$ to both the inhomogeneous and anisotropic tissue and to the isotropic and homogeneous one, Forchheimer’s correction produces, in the former case, a maximum difference between the magnitudes of the filtration velocity $\|\mathbf{q}\|$ and $\|\mathbf{q}_D\|$ of about 85%, and of about 60% in the latter. Thus, we may conclude that the more inhomogeneous and complex the microstructure is, the more Forchheimer’s correction could be significant in studying the flow. Indeed, it is possible that also this result is due to the microstructure as well as to a better resolution of the interplay between deformation and flow.

To test the FG-model of permeability, which takes the sample’s microstructure explicitly into account, we compared it with the AW-model. From the results of this comparison (see Fig. 6), we observed that the two models are discrepant in the Darcian case, but that the discrepancies can be partially smoothed over by modulating the AW-model with the aid of Forchheimer’s correction and, thus, of the friction factor. We believe that this behaviour could be due to the fact that Forchheimer’s correction introduces new parameters into the flow model, which can thus be employed to better fit experimental results. We emphasise that, by modulating the AW-model, we by no means intended to correct it. Rather, we chose to modulate the AW-model because, contrary to the FG-model, it is not restricted by the use of Darcy’s law at the REV scale. An important conclusion is that Forchheimer’s correction implies an increase of the fluid pressure and a dilation of the relaxation times for both the filtration velocity and pressure. This behaviour can be observed both in the equivalent scalar case and in the fully tensorial one (see Fig. 9).

In the future, we would like to study the combined effect of Forchheimer’s correction and the Brinkman equation to study the boundary effects on the fluid behaviour. These, indeed, may lead to a more precise description of the flow in complex benchmark tests, such as the indentation test.

Acknowledgements This work has been supported in part by the *Politecnico di Torino* (Italy) [AG] and [MC], in part by the *Fondazione Cassa di Risparmio di Torino* (Italy), through the “*La Ricerca dei Talenti*” (“HR Excellence in Research”) programme [AG] and in part by the Natural Science and Engineering Research Council of Canada, through the

NSERC Discovery Programme [SF]. Finally, we would like to acknowledge the contribution of Mr. Alberto Stracuzzi (former student of the *Politecnico di Torino*) to the material contained in Section 5.1 [45].

In Memoriam

In memory of our master Prof. Gaetano Giaquinta (1945–2016).

Compliance with Ethical Standards

The authors declare that they have no conflict of interest.

References

1. Ateshian, G.A., Weiss, J.A.: Anisotropic hydraulic permeability under finite deformation. *Journal of Biomechanical Engineering* **132**, 111,004–1–111,004–7 (2010)
2. Athanasiou, K.A., Darling, E.M., Hu, J.C.: Articular cartilage tissue engineering. *Synth. Lect. Tissue Eng.* **1**, 1–182 (2009)
3. Athanasiou, K.A., Rosenwasser, M.P., Buckwalter, J.A., Malinin, T.I., Mow, V.C.: Interspecies comparisons of in situ intrinsic mechanical properties of distal femoral cartilage. *J. Orthopaedic Research* **9**, 330–340 (1991)
4. Bear, J., Bachmat, Y.: Introduction to modeling of transport phenomena in porous media. Kluwer, Dordrecht, Boston, London (1990)
5. Bennethum, L.S., Giorgi, T.: Generalized Forchheimer equation for two-phase flow based on hybrid mixture theory. *Transport in Porous Media* **26**, 261–275 (1997)
6. Bennethum, L.S., Murad, M.A., Cushman, J.H.: Macroscale thermodynamics and the chemical potential for swelling porous media. *Transport in Porous Media* **39**, 187–225 (2000)
7. Bishop, R.L., Goldberg, S.I.: Tensor Analysis on Manifolds. Prentice-Hall, NJ, USA (1968)
8. Byrne, H., Preziosi, L.: Modelling solid tumour growth using the theory of mixtures. *Mathematical Medicine and Biology* **20**, 341–366 (2003)
9. Carfagna, M., Grillo, A.: The spherical design algorithm in the numerical simulation of biological tissues with statistical fibre-reinforcement. *Computing and Visualization in Science* **18**, 157–184 (2017)
10. Chen, S.S., Falcovitz, Y.H., Schneiderman, R., Maroudas, A., Sah, R.L.: Depth-dependent compressive properties of normal aged human femoral head articular cartilage: relationship to fixed charge density. *Osteoarthritis and Cartilage* **9**, 561–569 (2001)
11. Federico, S., Gasser, T.C.: Non-linear elasticity of biological tissues with statistical fibre orientation. *Journal of the Royal Society Interface* **7**, 955–966 (2010)
12. Federico, S., Grillo, A.: Elasticity and permeability of porous fibre-reinforced materials under large deformations. *Mechanics of Materials* **44**, 58–71 (2012)
13. Federico, S., Grillo, A., La Rosa, G., Giaquinta, G., Herzog, W.: A transversely isotropic, transversely homogeneous microstructural- statistical model of articular cartilage. *Journal of Biomechanics* **38**, 2008–2018 (2005)
14. Federico, S., Herzog, W.: On the anisotropy and inhomogeneity of permeability in articular cartilage. *Biomechanics and Modeling in Mechanobiology* **7**, 367–378 (2008)
15. Federico, S., Herzog, W.: On the permeability of fibre-reinforced porous materials. *International Journal of Solids and Structures* **45**, 2160–2172 (2008)
16. Grillo, A., Carfagna, M., Federico, S.: The Darcy-Forchheimer law for modelling fluid flow in biological tissues. *Theoret. Appl. Mech. TEOPM7* **41**(4), 283–322 (2014)
17. Grillo, A., Guaily, A., Giverso, C., Federico, S.: Non-linear model for compression tests on articular cartilage. *Journal of Biomechanical Engineering* **137**, 071,004–1–071,004–8 (2015)
18. Grillo, A., Logashenko, D., Stichel, S., Wittum, G.: Forchheimer's correction in modelling flow and transport in fractured porous media. *Computing and Visualization in Science* **15**, 169–190 (2012)
19. Hardin, R.H., Sloane, N.J.A.: McLaren's improved snub cube and other new spherical designs in three dimensions. *Discrete Computational Geometry* **15**, 429–441 (1996)
20. Hassanizadeh, S.M.: Derivation of basic equations of mass transport in porous media. Part 2. generalized Darcy's and Fick's laws. *Adv. Water Resour.* **9**, 208–222 (1986)
21. Hassanizadeh, S.M., Gray, W.G.: General conservation equations for multi-phase systems: 1. averaging procedure. *Adv. Water Resour.* **2**, 131–144 (1979)
22. Hassanizadeh, S.M., Gray, W.G.: General conservation equations for multi-phase systems: 2. mass, momenta, energy, and entropy equations. *Adv. Water Resour.* **2**, 191–203 (1979)
23. Hassanizadeh, S.M., Leijnse, A.: A non-linear theory of high-concentration-gradient dispersion in porous media. *Adv. Water Resour.* **18**(4), 203–215 (1995)
24. Hedlund, H., Mengarelli-Widholm, S., Reinholt, F., Svensson, O.: Stereological studies on collagen in bovine articular cartilage. *Acta Pathol. Microbiol. Immunol. Scand.* **101**, 133–140 (1993)
25. Holmes, M.H.: Finite deformation of soft tissue: analysis of a mixture model in uniaxial compression. *Journal of Biomechanical Engineering* **108**, 372–381 (1986)
26. Holmes, M.H., Mow, V.C.: The nonlinear characteristics of soft gels and hydrated connective tissues in ultrafiltration. *Journal of Biomechanics* **23**, 1145–1156 (1990)
27. Khaled, A., Vafai, K.: The role of porous media in modeling flow and heat transfer in biological tissues. *International Journal of Heat and Mass Transfer* **46**, 4989–5003 (2003)
28. Li, D., Engler, T.W.: Literature review on correlations of the non-darcy coefficient. *proceedings of the SPE Permian Basin Oil and Gas Recovery Conference*, Midland, Texas, 15–17 May 2001
29. Liu, I.S.: On representations of anisotropic invariants. *Int. J. Eng. Sci.* **20**(10), 1099–1109 (1982)
30. Mak, A.F., Lai, W.M., Mow, V.C.: Biphasic indentation of articular cartilage — i. theoretical analysis. *Journal of Biomechanics* **20**, 703–714 (1987)
31. Maroudas, A., Bullough, P.: Permeability of articular cartilage. *Nature* **219**, 1260–1261 (1968)
32. Marsden, J.E., Hughes, T.J.R.: *Mathematical Foundations of Elasticity*. Dover Publications, Inc., New York (1983)
33. McLaughlin, R.: A study of the differential scheme for the composite materials. *Int. J. Eng. Sci.* **15**, 237–244 (1977)

34. Mow, V.C., Holmes, M.H., Lai, M.W.: Fluid transport and mechanical properties of articular cartilage: a review. *Journal of Biomechanics* **17**, 377–394 (1984)
35. Mow, V.C., Kuei, S.C., Lai, W.M., Armstrong, C.: Biphasic creep and stress relaxation of articular cartilage in compression: Theory and experiments. *Journal of Biomechanical Engineering* **102**, 73–84 (1980)
36. Norris, A.N.: A differential scheme for the effective moduli of composites. *Mech. Mater.* **4**, 1–16 (1985)
37. Pierce, D.M., Ricken, T., Holzapfel, G.A.: A hyperelastic biphasic fibre-reinforced model of articular cartilage considering distributed collagen fibre orientations: continuum basis, computational aspects and applications. *Comput. Methods Biomech. Eng.* **16**, 1344–1361 (2013)
38. Pierce, D.M., Ricken, T., Holzapfel, G.A.: Modeling sample/patient-specific structural and diffusional responses of cartilage using dt-mri. *Int. J. Numer. Methods Biomed. Eng.* **29**, 807–821 (2013)
39. Podzniakov, S., Tsang, C.F.: A self-consistent approach for calculating the effective hydraulic conductivity of a binary, heterogeneous medium. *Water Resour. Res.* **40**, 1–13 (2000)
40. Quiligotti, S.: On bulk mechanics of solid-fluid mixtures: kinematics and invariance requirements. *Theoret. Appl. Mech.* **28**, 1–11 (2002)
41. Quiligotti, S., Maugin, G.A., dell'Isola, F.: An eshelbian approach to the nonlinear mechanics of constrained solid-fluid mixtures. *Acta Mech.* **160**, 45–60 (2003)
42. Quinn, T.M., Dierick, P., Grodzinsky, A.J.: Glycosaminoglycan network geometry may contribute to anisotropic hydraulic permeability in cartilage under compression. *J Biomech.* **34**(11), 1483–1490 (2001)
43. Rivlin, R.S., Ericksen, J.L.: Stress-deformation relations for isotropic materials. *J. Rational Mech. Anal.* **4**, 323–425 (1955)
44. Spencer, A.J.M.: Constitutive theory for strongly anisotropic solids. In: A.J.M. Spencer (ed.) *Continuum Theory of the Mechanics of Fibre-Reinforced Composites*, pp. 1–32. Springer-Verlag, Wien, Austria (1984). CISM Courses and Lectures No. 282, International Centre for Mechanical Sciences
45. Stracuzzi, A.: *Stime dell'influenza della correzione di Forchheimer nei modelli bifasici della cartilagine articolare*. MSc Thesis, Politecnico di Torino (In Italian) (2015)
46. Thauvin, F., Mohanty, K.K.: Network modeling of non-darcy flow through porous media. *Transport in Porous Media* **31**, 19–37 (1998)
47. Tomic, A., Grillo, A., Federico, S.: Poroelastic materials reinforced by statistically oriented fibres - numerical implementation and application to articular cartilage. *IMA Journal of Applied Mathematics* **79**, 1027–1059 (2014)
48. Torzilli, P.A., Mow, V.C.: On the fundamental fluid transport mechanisms through normal and pathological articular cartilage during function - I - the formulation. *Journal of Biomechanics* **9**, 541–552 (1976)
49. Torzilli, P.A., Mow, V.C.: On the fundamental fluid transport mechanisms through normal and pathological articular cartilage during function - II - the analysis, solution and conclusions. *Journal of Biomechanics* **9**, 587–606 (1976)
50. Walpole, L.J.: Elastic behavior of composite materials: Theoretical foundations. *Advances in Applied Mechanics* **21**, 169–242 (1981)
51. Walpole, L.J.: Fourth-rank tensors of the thirty-two crystal classes: Multiplication tables. *Proceedings of the Royal Society of London Series A* **391**, 149–179 (1984)
52. Wang, X., Thauvin, F., Mohanty, K.K.: Non-darcy flow through anisotropic porous media. *Chemical Engineering Science* **54**, 1859–1869 (1999)
53. Whitaker, S.: The forchheimer equation: A theoretical development. *Transport in Porous Media* **25**, 27–61 (1996)
54. Wu, J.Z., Herzog, W.: Finite element simulation of location- and time-dependent mechanical behavior of chondrocytes in unconfined compression tests. *Ann. Biomed. Eng.* **28**, 318–330 (2000)